Tectonophysics 721 (2017) 123–142

Contents lists available at ScienceDirect

Tectonophysics

journal homepage: www.elsevier.com/locate/tecto

Hydraulic properties of a low permeable rupture zone on the Yingxiu-Beichuan Fault activated during the Wenchuan earthquake, China: Implications for fluid conduction, fault sealing, and dynamic weakening mechanisms

Qingbao Duan[a,*], Xiaosong Yang[a], Jianye Chen[b]

[a] State Key Laboratory of Earthquake Dynamics, Institute of Geology, China Earthquake Administration, Beijing, China
[b] HPT Laboratory, Department of Earth Sciences, Utrecht University, Utrecht, The Netherlands

ARTICLE INFO

Keywords:
Yingxiu-Beichuan Fault
Fault rocks
Hydraulic properties
Fault healing
High pore pressure
Thermal pressurization

ABSTRACT

Fluid transport properties of fault rocks are crucial parameters that affect earthquake nucleation and rupture propagation. In this study, we examined the internal structure, mineral composition and fluid transport properties of fault rocks collected from two shallow boreholes penetrating a granitic rupture zone on the Yingxiu-Beichuan Fault (YBF) that was activated during the 2008 Wenchuan earthquake. Fluid transport properties were measured using water as pore fluid at effective pressures (P_e) ranging from 10 MPa to 165 MPa. Permeabilities of fault rocks exhibit a wide variation from 2.1×10^{-22} m^2 to 4.6×10^{-17} m^2, strongly depending on rock types and overburden pressure. Specifically, at P_e of 165 MPa, the damage zone samples have permeabilities from 5.0×10^{-21} m^2 to 1.2×10^{-17} m^2, and the fault gouges are between 2.1×10^{-22} m^2 and 3.1×10^{-19} m^2. Thus, the YBF consists of a low-permeability fault core acting as fluid barrier, and surrounding high-permeability damage zones acting as fluid conduits. Combining the structural and compositional results and transport data together, we propose that the interplay between cataclasis and fluid-rock interactions controls the hydraulic properties and their response to the fault zone evolution. It is noteworthy that we measured extremely low permeabilities but high porosities and high specific storages for the gouges. The cemented cataclasites, which are inferred to be equivalent to the rocks in which the Wenchuan earthquake nucleated also have low permeabilities, suggesting the fault zone is a potential area for fluid storage and capable of generating high pore pressure at depths. According to our laboratory data, we found fluid pressurization could occur at depths below 2.7 km. We suggest thermal pressurization has played an important role in causing the dynamic weakening of the Wenchuan earthquake.

1. Introduction

Fault zones have been demonstrated as areas favoring crustal fluid migration (Morrow et al., 1981; Sibson, 1992; Rice, 1992; Byerlee, 1993). Fluids within fault zones are intimately related to fault behavior and faulting processes, and hence have attracted great interests in recent years (e.g., Hickman et al., 1995; Polak et al., 2003; Wibberley and Shimamoto, 2005; Rice, 2006). Permeability is a primary parameter controlling fluid transport and fluid-rock interaction behaviors that affect the strength of faults and faulting processes. For example, the buildup of high pore pressure can significantly weaken a fault and cause the nucleation of mega-earthquakes, especially in thrust fault systems (e.g., Hickman et al., 1995). In particular, for a high-angle thrust earthquake, it has been generally considered to occur in the presence of excess pore pressure (Sibson et al., 1988). In addition, coseismic frictional heating can generate a transient increase in fluid pressure due to thermal pressurization and dehydration reactions, which promote fault slip and accelerate rupture propagation (Sibson, 1973; Mase and Smith, 1987; Noda and Shimamoto, 2005). Fluids contained in fault zones can also react efficiently with fault rocks due to their fine grain size and large surface area, producing phyllosilicates (e.g., Wintsch et al., 1995) that usually have low frictional strength and low permeability (Behnsen and Faulkner, 2011). As such fluid alteration proceeds, not only chemical compositions but also fluid transport properties of fault rocks will concomitantly change (Wu, 1978; Solum et al., 2006; Molli et al., 2010).

* Corresponding author.
E-mail addresses: duan_qingbao@126.com (Q. Duan), xsyang@ies.ac.cn (X. Yang), jychen@ies.ac.cn (J. Chen).

http://dx.doi.org/10.1016/j.tecto.2017.10.002
Received 6 March 2017; Received in revised form 26 September 2017; Accepted 1 October 2017
Available online 02 October 2017

Hydraulic structures of fault zones strongly depend on fault zone architectures and fault rock distributions. Large mature fault zones usually have complicated structures, depending on their active-quiescent history and accumulated deformation that the faults have accommodated. Based on field and laboratory studies, the upper crustal fault zones are generally divided into fault cores, surrounding damage zones, and host rocks (Chester and Logan, 1986; Chester et al., 1993; Caine et al., 1996; Lockner et al., 2000). Fault cores represent the place where most of the displacements accumulated, are characterized by fine-grained fault gouges, relatively low shear strength (e.g., Zhang and He, 2013), and low permeability (e.g., Faulkner and Rutter, 2000; Morrow et al., 2014). Faulkner et al. (2010) further classified fault zone structures into two typical types: 1) a simple fault core and damage zones and 2) a combined damage zones with multiple cores. Permeabilities of fault rocks across a fault zone vary with the grain size, mineral compositions and deformation processes of each unit (Wibberley and Shimamoto, 2003; Faulkner et al., 2010). Caine et al. (1996) proposed a simple conduit/barrier permeability structure across a fault zone, with the low permeable fault core serving as a barrier and high permeable damage zones on two sides as fluid conduits. Permeability structure of seismogenic fault zones such as the Nojima fault (Lockner et al., 2000; Mizoguchi et al., 2008), the Chelungpu fault (Tanikawa and Shimamoto, 2009), the East Fork thrust fault (Evans et al., 1997), and the Yingxiu-Beichuan Fault (YBF) (Chen et al., 2011) generally conform to such conduit/barrier binary system. However, there are also some exceptions that show strong complexity across the faults such as the Median Tectonic Line of Japan (Wibberley and Shimamoto, 2003), the Carboneras fault (Faulkner et al., 2003), and the San Andreas fault (Morrow et al., 2014). In these fault zones, contrasting host rock lithology and multiple slip zones were observed. These characters lead to the permeability architecture across such faults varying significantly.

On 12 May 2008, the catastrophic Wenchuan earthquake occurred on the YBF and produced a 240 km-long rupture zone, cutting through several lithological units along its strike. The maximum coseismic vertical slip offset caused by this quake is ~9 m (Ran et al., 2010). The depth of hypocenter was around 19 km (Chen et al., 2009), and an average stress drop of 18 MPa was approached during coseismic slip (Zhang et al., 2009). In view of the large coseismic displacement and large stress drop associated with the Wenchuan earthquake, dynamic slip weakening mechanisms must have played an important role in causing the coseismic rupture propagation. After this quake, various laboratory studies have been carried out to study the mechanical and fluid transport properties of this host fault, on fault rocks collected from surface ruptures (Chen et al., 2011; Yang et al., 2012; Chen et al., 2013a, 2013b; Yao et al., 2013; Zhang and He, 2013), shallow (Xiaojiaqiao borehole (site 5 in Fig. 1): 85 m depth, Hou et al., 2012; Golden river borehole (site 4 in Fig. 1): 134 m depth, Duan et al., 2016; Yang et al., 2016) and deep (WFSD-1 at Baojiaomiao (site 3 in Fig. 1): 1200 m depth, Li et al., 2013; Xue et al., 2013) drilling campaigns. It has been suggested that host rock lithology is important in controlling the fluid transport properties of faults (e.g., Mizoguchi et al., 2008). Previous studies are mostly focusing on the segments where clastic sedimentary and carbonate rocks hosted (Verberne et al., 2010; Hou et al., 2012; Chen et al., 2013a, 2013c; Yao et al., 2013; Zhang and He, 2013), however studies on the crystalline unit (Fig. 1, the Pengguan complex) which has been inferred as the source rocks at rupture nucleation depth (e.g., Chen et al., 2009) are still rare (Chen et al., 2016).

In the present study, to understand the internal and hydraulic structures as well as fluid-involved processes in the YBF, we performed field and laboratory studies on a granitic unit of the Pengguan Complex, at the Golden River (GR) site (Fig. 1). Representative samples of typical host and fault rocks were collected from the surface outcrop and from two shallow boreholes that penetrate the fault zone. Detailed microstructural, mineralogical analyses and fluid transport properties (including permeability, porosity, and specific storage) measurements were performed. Incorporating the results obtained, we discussed the hydraulic fluid conduction features and sealing mechanisms involved in the fault rocks. Finally, we further investigated the possibility that thermal pressurization occurred during the Wenchuan earthquake based on our experimental data.

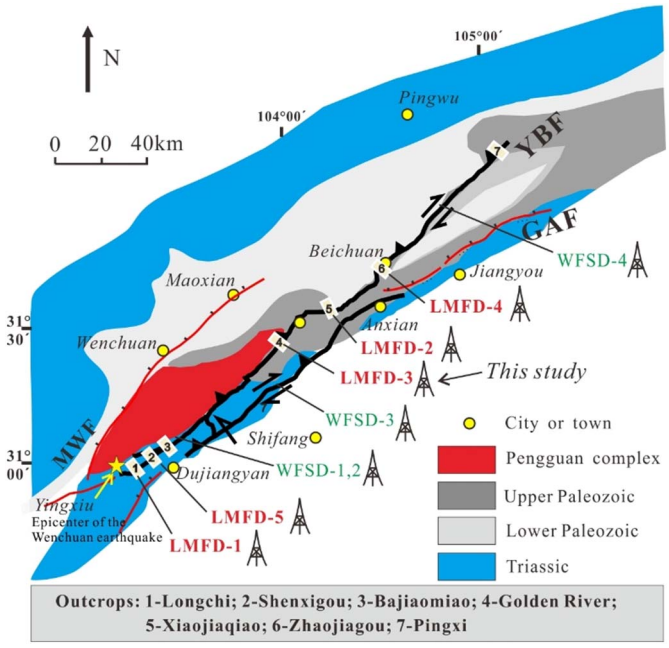

Fig. 1. Regional geological background of the Longmenshan Fault Zone (Modified after Chen et al., 2013b and Duan et al., 2016). The thick black lines denote the coseismic surface ruptures of the Wenchuan earthquake. MWF, Maoxian-Wenchuan Fault; YBF, Yingxiu-Beichuan Fault; GAF, Guanxian-Anxian Fault. LMFD, Longmenshan Fault Shallow Drilling Project (Duan et al., 2016); WFSD, Wenchuan Earthquake Fault Scientific Drilling Project (Li et al., 2013). Locations of the WFSD and LMFD drilling sites and representative surface outcrops of the YBF are marked on the map. In this study, we focus on the Golden River site (LMFD-3, site 4).

2. Geological setting

2.1. Longmenshan Fault Zone

The Longmenshan Fault Zone (LFZ) consists of the Maoxian-Wenchuan Fault, Yingxiu-Beichuan Fault (YBF), and Guanxian-Anxian Fault, is located between the east margin of the Tibetan Plateau and the Sichuan basin (Fig. 1). Geomorphology and chronology studies have shown that slip rate of the Longmenshan fault is 2–3 mm/yr in the late Quaternary period (Xu et al., 2005). The 2008 Wenchuan earthquake ruptured the YBF and the Guanxian-Anxian Fault (Xu et al., 2009). The coseismic slip consists of thrust- and right-slip components, with the maximum vertical and horizontal offsets measured to be 6.5 m and 4.9 m, respectively (Xu et al., 2009). Both field geological observation (Xu et al., 2009) and geophysical inversion (Zhang et al., 2009) results have shown that the coseismic displacements and slip velocities for the northern and southern portions of the rupture zone are characterized by segmentation and variations for each segment. Thrust- and right-slip components along the southern part of the YBF are comparable, but right-slip dominates the northern part of the fault.

From SW to NE, several strata with various lithologies host the YBF. The southern segment of the YBF is hosted by Proterozoic Pengguan complex and Triassic Xujiahe formation sedimentary rocks (i.e., carbonate rocks, clastic sedimentary rocks, and volcanic rocks). Host rocks in the middle segment of the YBF consist of Paleozoic limestone, dolomite, and Triassic thick layers of limestone and clastic sedimentary rocks. While in the northern portion, the YBF cuts Paleozoic strata, including dolomitic limestone, sandstone, and carbonaceous shale (Burchfiel et al., 1995).

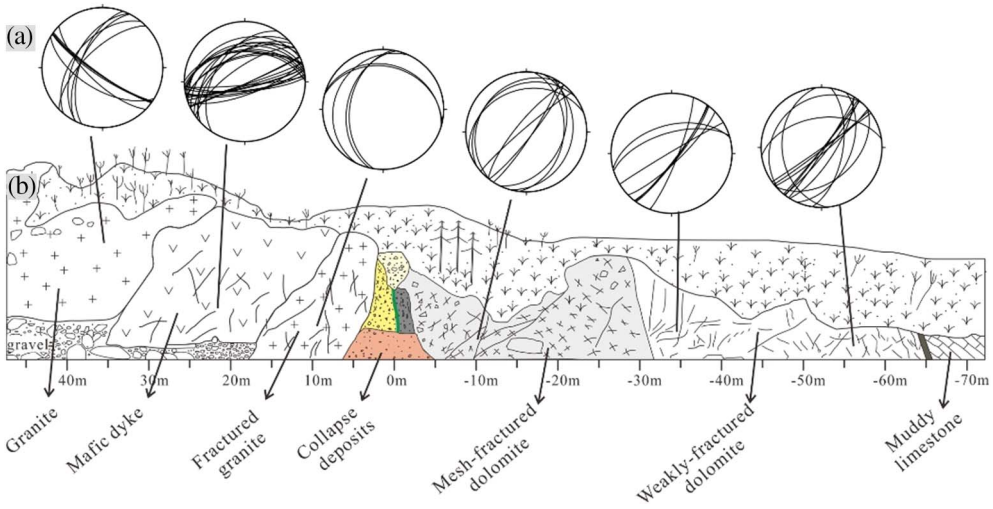

Fig. 2. Lower hemisphere projection of the joints (a), and an interpretive sketch of the Golden River outcrop (b) traced from the photograph of fig. 3a.

2.2. Golden River outcrop

The GR outcrop (31°27′41″ N, 103°59′56″ E) is located along the middle segment of the YBF (Fig. 1). Here, the coseismic slip cuts through granitic rocks, with hanging wall within the Neoproterozoic (859–699 Ma) Pengguan complex (Ma et al., 1996; Zhang et al., 2008) and footwall consisting of Upper Paleozoic carbonate-related strata. The fault here strikes 40° and dips 70°–87° SE with fault plane exhibiting slightly reversed inclination at the surface (Duan et al., 2016). The coseismic vertical slip offset around the GR site was ~3.4 m thrust motion (Xu et al., 2009). Conjugate shear joints developed in the fault zone are used to infer the stress field (Engelder, 1987; Hancock et al., 1991). The lower hemisphere projections of the joints are presented in Fig. 2a. Results show that the direction of maximum principal stress in the hanging wall host rocks is SW-NE, and gradually changed into NW-SE in the damage zones and footwall rock, reflecting a compressional maximum stress acting on the fault zone. This is consistent with the regional geological background of continuous thrust fault movement in the LFZ (e.g., Burchfiel et al., 1995).

At the GR site, an almost 2-km long fault zone outcrop is exposed along a river valley. The hanging wall is about 1.5 km along the upstream direction and footwall is about 500 m along the downstream direction of the river. Different units across the fault zone were distinguished following Caine et al. (1996). As shown in Fig. 2 of Duan et al. (2016), the fault zone is composed mainly of the damage zones and a nearly 3.3 m wide fault core. The width of the hanging wall damage zone is ~10 m, and that of the footwall is ~63 m. The fault core is composed primarily of three gouge layers with distinct colors and an about 1-m-thick fine-grained granitic breccia zone. The yellow-green gouge (YGG) and grey-green gouge (GGG), with a total thickness of ~20 cm, can be distinguished and well traced along the fault plane. The black gouge (BG) is ~2 m-thick and contains two cataclastic lenses. Damage zone on the west side of the fault core is composed of fractured and altered granite, granitic breccia and black granitic cataclasite. The black cataclasite is highly fractured with a small amount of fine-grained granitic breccia scattered in it. Damage zone on the east side of the fault core is mainly composed of dolomitic cataclasite and variably fractured dolomite. Despite the heterogeneity of fracture and deformation across the fault zone, a general increase in cataclastic fracturing intensity occurs toward the fault core. From NW to SE (Figs. 2 and 3), the exposed host rocks and fault rocks at the GR outcrop are (1) granite, (2) mafic dyke, (3) fractured granite, (4) black cataclasite, (5) granitic breccia, (6) YGG, (7) GGG, (8) BG, (9) dolomitic cataclasite, (10) mesh-fractured dolomite, (11) weakly fractured dolomite, and (12) muddy limestone. Based on the crosscutting relationships, distinct mineral compositions and deformation structures of the gouges, the 2008 Wenchuan earthquake was inferred to be passing through the YGG (Duan et al., 2016).

Two shallow boreholes were performed at the GR outcrop, which located 42 m (hole-A) and 15 m (hole-B) west of the principal slip zone (PSZ) (Fig. 3), respectively. Detailed information about the boreholes and drilling cores have been reported by Duan et al. (2016), only a brief introduction is shown here. The first one (hole-A), with a total depth of 134 m, penetrated the granite host rock, mafic dyke and granitic cataclasite, but unfortunately, it did not penetrate the fault core because of difficulties during the drilling operation. The second one (hole-B), with a total depth of 54 m, was set directly on top of the granite, and it intersected the fault core. A comparable rock sequence was observed in the boreholes and the surface outcrop, indicating that the rocks can be traced along the dip direction at least within the depth extent of the drilling (Fig. 3).

3. Experimental samples

3.1. Sampling method

The experimental samples (Table 1) were collected from the outcrop and drilling cores. The boreholes did not penetrate the footwall, and therefore the footwall carbonates were taken from the surface outcrop instead. All the samples are labeled in Fig. 3. Cylindrical samples with a diameter of 20 mm and length of 5–20 mm were prepared for hydraulic properties measurement experiments. For incohesive samples like fault breccias and gouges, thin-walled (0.1 mm in thickness) copper tubes of 20 mm in diameter were inserted into the drilling cores and extracting them with the enclosed material. For cohesive rocks like host rocks and cataclasites, coring was done in the laboratory on the drilling cores or hand specimens (footwall rocks) collected in the field. Samples from the drilling cores were collected perpendicular to the axis of the boreholes. Both end surfaces of the cylindrical samples were cut or polished to be parallel to each other. Before experiments, samples were oven dried at 60 °C for ~72 h to eliminate pore water.

3.2. Sample description

3.2.1. Cohesive rocks (host rocks and cataclasites)

Photographs of the cylindrical experimental samples of cohesive rocks were scanned by a high precision scanner. They are included in Fig. 4 to illustrate their textural features. These cohesive rocks are classified into three types (intact host rocks, cataclasites, and mesh-fractured cataclasites) according to their crack development and cementation degree to reflect different hydraulic conduction features.

Host rocks (Fig. 4a, b, c), including the granites and mafic dyke from

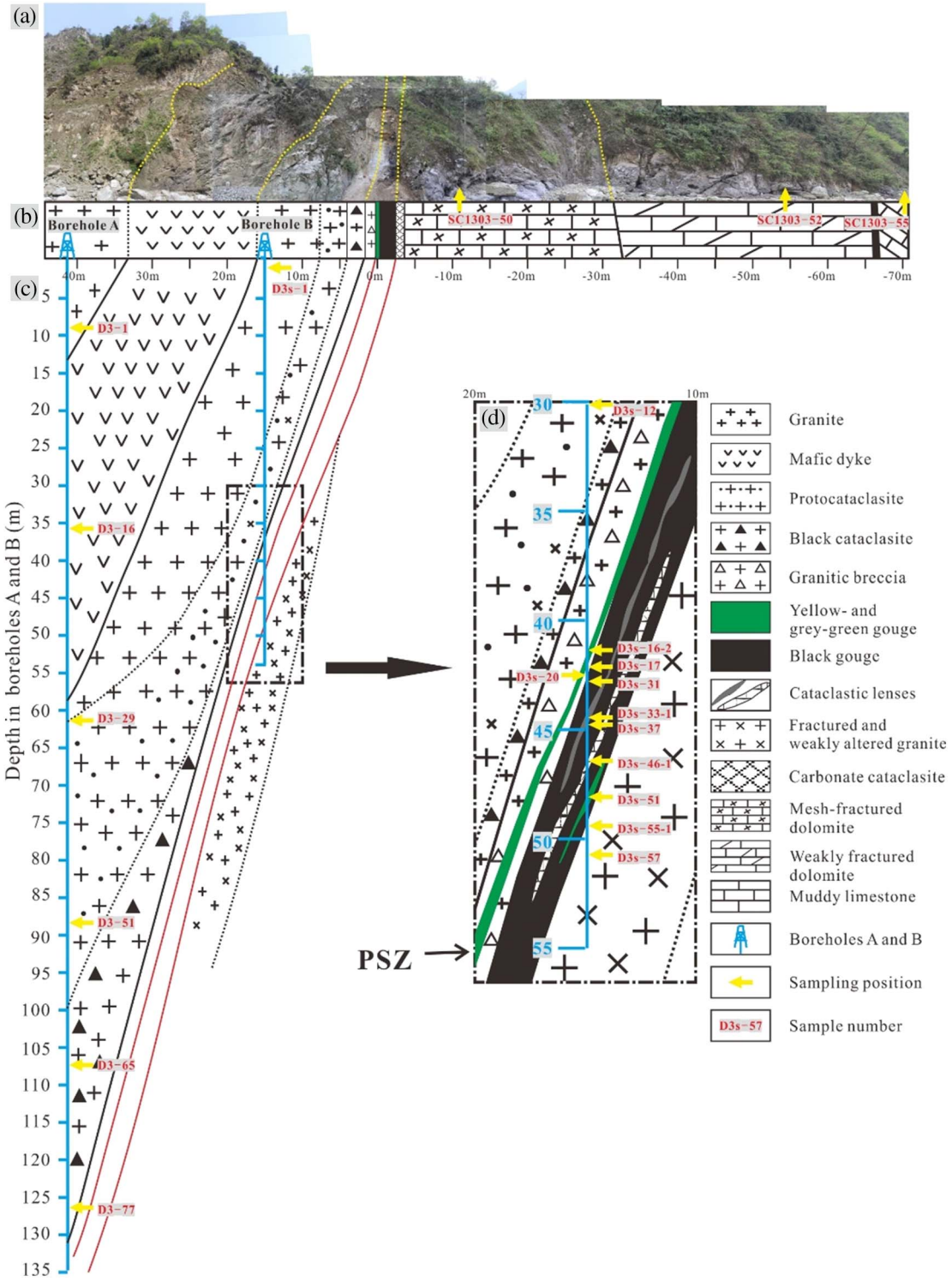

Fig. 3. Lithological profiles of the Golden River fault zone revealed by surface outcrop and drilling cores (modified from Duan et al., 2016). (a) Photograph of the surface outcrop. (b) Interpretive sketch of the outcrop focusing on the lithologies across the outcrop. (c) Depth profile revealed by the drilling cores. (d) Enlargement of the rectangle area in (c) illustrating the internal structure of the fault zone revealed in hole-B. Principal slip zone (PSZ) of the 2008 Wenchuan earthquake was inferred passing through the yellow-green gouge (Duan et al., 2016). The yellow arrows indicate the sampling positions in this study. (For interpretation of the references to color in this figure legend, the reader is referred to the web version of this article.)

the Pengguan complex, are generally well crystallized and show more or less a homogeneous texture. Cracks are rarely seen in them. These samples specify the host rocks that are intact and do not show any obvious evidence of damage.

Cataclasites including a sample that is originally granite (Fig. 4d) taken from the hanging wall damage zone, a sample (Fig. 4e) cored from a lens wrapped in the BG zone, and a footwall muddy limestone (Fig. 4f). Cracks in the footwall muddy limestone sample are visible but have generally been filled with mineral veins (Fig. 4f). This type of samples represents the cataclasites that have experienced multiple healing and sealing processes. Fluid migration relics, calcite veins, and black carbonaceous materials are found to be the most common

Table 1
Samples and key experimental results.

Sample no.	Sample position	Rock type	Initial porosity[a]	Permeability (m^2)						
				P_0 = 10 MPa	P_e = 10–65 MPa		P_0 = 85 MPa	P_e = 85–165 MPa		P_e = 165 MPa
				k_0	γ	R^2	k_0	γ	R^2	k
D3-1	9.60 m in hole-A	Granite	1.28%	6.96×10^{-20}	0.0655	0.9915	8.94×10^{-22}	0.0191	0.9941	2.47×10^{-22}
D3-16	35.50 m in hole-A	Mafic dyke	–	4.30×10^{-22}	–		–	–		–
D3-29	60.14 m in hole-A	Granitic cataclasite	2.67%	4.28×10^{-20}	0.0229	0.9970	9.69×10^{-21}	0.00848	0.9980	4.97×10^{-21}
D3-51	88.46 m in hole-A	Black granitic cataclasite	1.71%	1.01×10^{-18}	0.0453	0.9910	6.12×10^{-20}	0.0232	0.9806	1.25×10^{-20}
D3-65	107.61 m in hole-A	Black granitic cataclasite	1.17%	1.72×10^{-18}	0.0470	0.9708	7.16×10^{-20}	0.0243	0.9840	1.32×10^{-20}
D3-77	126.50 m in hole-A	Black granitic cataclasite	1.20%	4.11×10^{-18}	0.0253	0.9894	1.17×10^{-18}	0.0185	0.9681	1.61×10^{-19}
D3s-1	3.90 m in hole-B	Granite	–	1.03×10^{-20}	0.0411	0.9984	4.37×10^{-22}	0.0173	0.9663	–
D3s-12	30.62 m in hole-B	Granitic coarse breccia	2.75%	1.10×10^{-17}	0.0308	0.9668	1.17×10^{-18}	0.0185	0.9895	3.07×10^{-19}
D3s-16-2	42.00 m in hole-B	Yellow-green gouge	15.71%	4.99×10^{-19}	0.0583	0.9866	2.30×10^{-20}	0.0171	0.9965	5.93×10^{-21}[b]
D3s-17	42.12 m in hole-B	Fine-grained granitic breccia	13.26%	1.62×10^{-21}	0.0187	0.8770	5.85×10^{-22}	0.00677	0.9986	3.39×10^{-22}
D3s-20	42.31 m in hole-B	Fine-grained granitic breccia	17.16%	9.41×10^{-19}	0.0564	0.9859	3.49×10^{-20}	0.0193	0.9879	6.95×10^{-21}
D3s-31	43.17 m in hole-B	Black gouge	20.97%	1.36×10^{-21}	0.0190	0.9634	3.72×10^{-22}	0.00489	0.9772	2.14×10^{-22}
D3s-33-1	43.88 m in hole-B	Granitic cataclasite	5.18%	5.80×10^{-21}	0.0062	0.9214	3.84×10^{-21}	0.00366	0.8066	2.76×10^{-21}
D3s-37	44.41 m in hole-B	Black gouge	19.14%	2.75×10^{-21}	0.0313	0.9033	6.83×10^{-22}	0.0110	0.9080	3.03×10^{-22}
D3s-46-1	45.66 m in hole-B	Dolomitic cataclasite	9.95%	2.47×10^{-17}	0.0100	0.8076	1.47×10^{-17}	0.0022	0.8827	1.20×10^{-17}
D3s-51	47.39 m in hole-B	Grey-green gouge	16.42%	2.87×10^{-18}	0.0832	0.9995	1.95×10^{-20}	0.0245	0.9995	2.63×10^{-21}
D3s-55-1	48.70 m in hole-B	Black gouge	16.42%	1.38×10^{-19}	0.0800	0.8878	1.36×10^{-21}	0.0180	0.9766	3.38×10^{-22}
D3s-57	51.29 m in hole-B	Fine-grained granitic breccia	14.35%	1.28×10^{-20}	0.0650	0.8730	9.12×10^{-22}	0.0156	0.9265	2.90×10^{-22}
SC1106-14	70 m in outcrop	Granite	–	8.08×10^{-20}	0.0476	0.9915	6.52×10^{-21}	0.0269	0.9901	1.10×10^{-21}
SC1303-50	− 11 m in outcrop	Dolomitic cataclasite	1.27%	9.14×10^{-19}	0.0314	0.9791	1.71×10^{-19}	0.00896	0.9769	8.93×10^{-20}
SC1303-52	− 54 m in outcrop	Dolomitic cataclasite	2.20%	4.19×10^{-17}	0.0430	0.6829	9.64×10^{-18}	0.0102	0.9966	4.18×10^{-18}
SC1303-55	− 71 m in outcrop	Muddy limestone	2.39%	2.64×10^{-18}	0.0771	0.9997	1.56×10^{-20}	0.0182	0.9715	3.23×10^{-21}

R^2 is correlation coefficient that denotes the goodness of curve fitting. "P_e", effective pressure; "–", denotes below the lower limit of measurement.
[a] Initial porosity was measured under 10 MPa effective pressure with nitrogen gas as the pore fluid.
[b] The permeability data of the yellow-green gouge at 165 MPa P_e was previously reported by Duan et al., 2016.

cementing and void-infilling materials.

Mesh-fractured cataclasites are originally cataclasites and currently contain fracture networks, probably due to the damage along the exhumation to the subsurface from their forming depths. Two typical examples are the black granitic cataclasites in the hanging wall damage zone and dolomitic cataclasites in the footwall. The black cataclasites are strongly damaged, with fractures and cracks visible in both hand specimen- and micro-scales (Fig. 4g, h and i). Anastomosing compaction shear bands occasionally appear, where grains are extremely fractured. Feldspar and biotite are extensively altered in these samples, with the secondary minerals such as kaolinite, zeolite and chlorite being precipitated in the fractures (Duan et al., 2016). For the footwall dolomitic cataclasites, rare alteration products are present in the fractures (Fig. 4j, k, l). Black carbonaceous materials are found to be present in the fractured cataclasites, usually distributing along the cracks (Fig. 4g, h, i and k).

3.2.2. Incohesive rocks (fault breccias and fault gouges)

Toward the fault core, fault rock samples show gradually enhanced degree of fracturing and fluid-rock interaction. Representative microphotographs of incohesive fault breccias and gouges taken from the fault core are shown in Fig. 5. These samples are featured by fine grain size, matrix-supported structure, and extensive mineral alteration and precipitation, which are remarkably different from the cohesive rocks (Fig. 4). Detailed descriptions for the fault breccias and fault gouges have been provided by Duan et al. (2016), and here we give a brief description, mainly focusing on the fluid-related microstructures.

The fine-grained granitic breccia is composed of fragments and surrounding fine-grained matrix. Most feldspars in the granitic breccia are replaced by mica or clay minerals. The neo-formed fine-grained materials wrap around the surviving clasts and constituting a matrix-supported texture. Multiple episodes of micro-fractures and micro-faults, which are filled with mica or phyllosilicate minerals or healed by calcite, can be observed (Duan et al., 2016). The grain boundaries develop many micro-pores (Fig. 5a).

All three gouges were used for our experiments; they are the YGG, GGG, and BG (Figs. 5, 6). The gouges are composed mainly of fine-grained matrix and randomly-distributed rock clasts. The matrix is composed primarily of clay minerals and scarce fine-grained quartz. The clasts consist of crushed quartz, carbonates, and feldspars. In general, all the gouge samples show a typical matrix-supported structure, with minor fractured clasts surrounded by fine-grained clay matrix. The YGG consists mainly of quartz clasts and greenish clay-sized materials with a small number of feldspars. Micro-shear bands, flow structures, and reworked mafic clasts are discerned in the YGG (Fig. 5b, also see Fig. 7d and e of Duan et al., 2016). The BG characterized by the development of foliation and layers of interleaved hydrothermal veins is composed mainly of quartzitic porphyroclasts and a minor amount of carbonate clasts surrounded by gouge matrix (Duan et al., 2016) (Fig. 5c, d, e, and Fig. 6b). Foliation is discerned by color bending in the matrix and by crushed particles that are aligned along localized shear bands. Fine-grained phyllosilicates are well developed, and micro-pores are present between the phyllosilicate layers (Fig. 5d).

Furthermore, injection of gouge veins (Fig. 6a) and clay-clast aggregates (CCAs, Fig. 5e, Boutareaud et al., 2010) were seen in the gouges. The widespread calcite vein cementation (Fig. 6b, c), the formation of clay minerals and precipitation of pyrite (Fig. 5b, f) as well as the development of carbonaceous materials (Fig. 6d) indicate complex healing processes in the fault zone. In addition, pressure solution seams and grain size reduction are found in the fault rocks (Fig. 6e, f).

4. Experimental methods

4.1. Mineralogical analysis

X-ray Diffraction (XRD) method was employed to examine the mineral assemblages of the samples, including the bulk-rock composition and semi-quantitative clay composition. Quantitative mineral proportion measurement in this study is based on the fact that the peak intensities from an individual mineral can be correlated to the mineral content in the sample. The relative weight percent of certain mineral phase in a sample is proportional to the intensity of a reflection of this

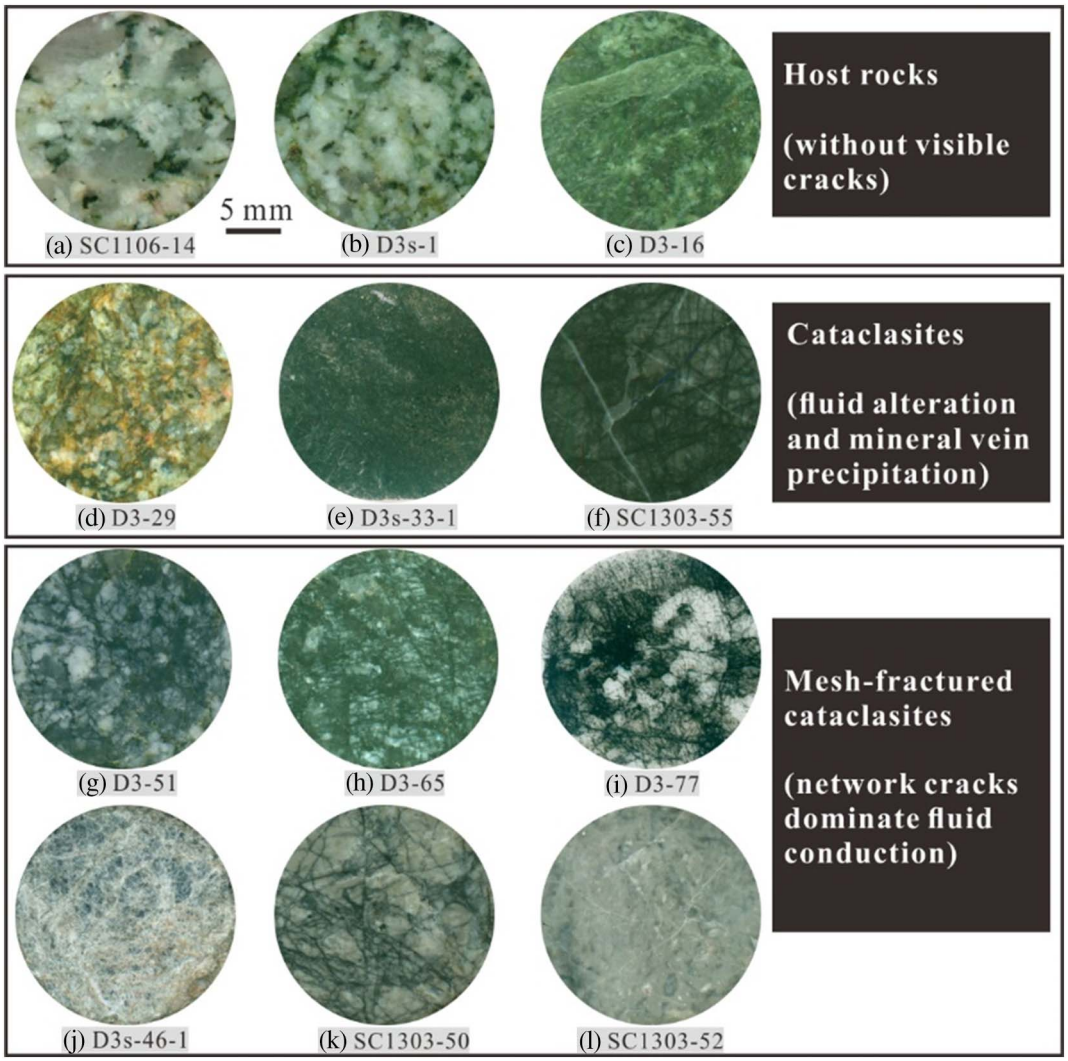

Fig. 4. Representative scanned photos of the cohesive samples showing their textural features. These cohesive samples are classified into three types, namely intact host rocks, cataclasites, and mesh-fractured cataclasites, according to their crack development and cementation degree. (a–b) granite host rocks, (c) mafic dyke, (d–e) granitic cataclasites, (f) muddy limestone cataclasite, (g–i) black granitic cataclasites, and (j–l) dolomitic cataclasites.

component in the XRD pattern. In this study, normalized reference intensity ratio method (Hubbard et al., 1976) was used for our quantitative XRD analysis, and corundum was selected as the reference standard. Crushed and milled powder samples with grain size < 200 meshes were scanned using a Dmax X-ray powder diffractometer (12 kW, 45 kV and 100 mA) with 2θ ranging from 3° to 45° under a step size of 0.02° and scan rate of 2°/min by CuK-α radiation (0.15418 nm). For identifying the clay minerals, centrifugation separated clay-sized portions (< 2 μm) were further analyzed. Suspensions of < 2 μm fraction were air-dried on glass slides, and ethylene glycol was added to detect swelling components (smectite). Then, the samples were heated to 550 °C to distinguish kaolinite from chlorite. The peaks used for estimate the relative content of clay minerals were illite (10 Å), chlorite (14.2 Å), kaolinite (7 Å), and illite/smectite 001/001 (x > 10 Å) upon glycolation. The relative content of kaolinite and chlorite were determined by the peak intensity ratio at 3.58 and 3.53 Å (Solum et al., 2003). The smectite fraction was deduced from the intensity of the 10 Å peak on air-dried and 17 Å peak on ethylene glycol samples.

4.2. Fluid transport properties measurements

Fluid transport properties (permeability, porosity, and specific storage) measurements were performed at room temperature and intravessel confining pressure conditions, employing a fluid flow apparatus installed at the Institute of Geology, China Earthquake Administration. By using different fluid reservoirs, either gas or liquid can work as pore fluid. Through an intensifier, the confining pressure can reach to 200 MPa. The pore pressure is generated by two motor-controlled syringe pumps that can provide fluid flow under conditions of constant flow rate, constant differential pressure or sinusoidal oscillating pressure, and therefore both steady-state flow and pore pressure oscillation (PPO) methods are available for permeability measurement on this apparatus (see Chen et al., 2015 for details).

Due to the ultra-low permeable nature of clay gouges, the PPO method was chosen for our experiments (Kranz et al., 1990; Fischer and Paterson, 1992). Measurements were performed at cycling confining pressure ranging from 25 MPa to 180 MPa, with distilled water as pore fluid at a mean pressure of 15 MPa for the oscillation. Based on the data of amplitude attenuation and phase difference of pore pressures recorded at upstream and downstream reservoirs (Fig. 7), the permeability and specific storage of a specimen can be calculated at each confining pressure according to the method given by Fischer and Paterson (1992).

Initial porosity of a sample was determined by the Boyle-Mariotte law (isothermal gas state equation) with nitrogen gas as the pore fluid. Before the experiment, the volumes of two enclosed pipelines (V_1 and

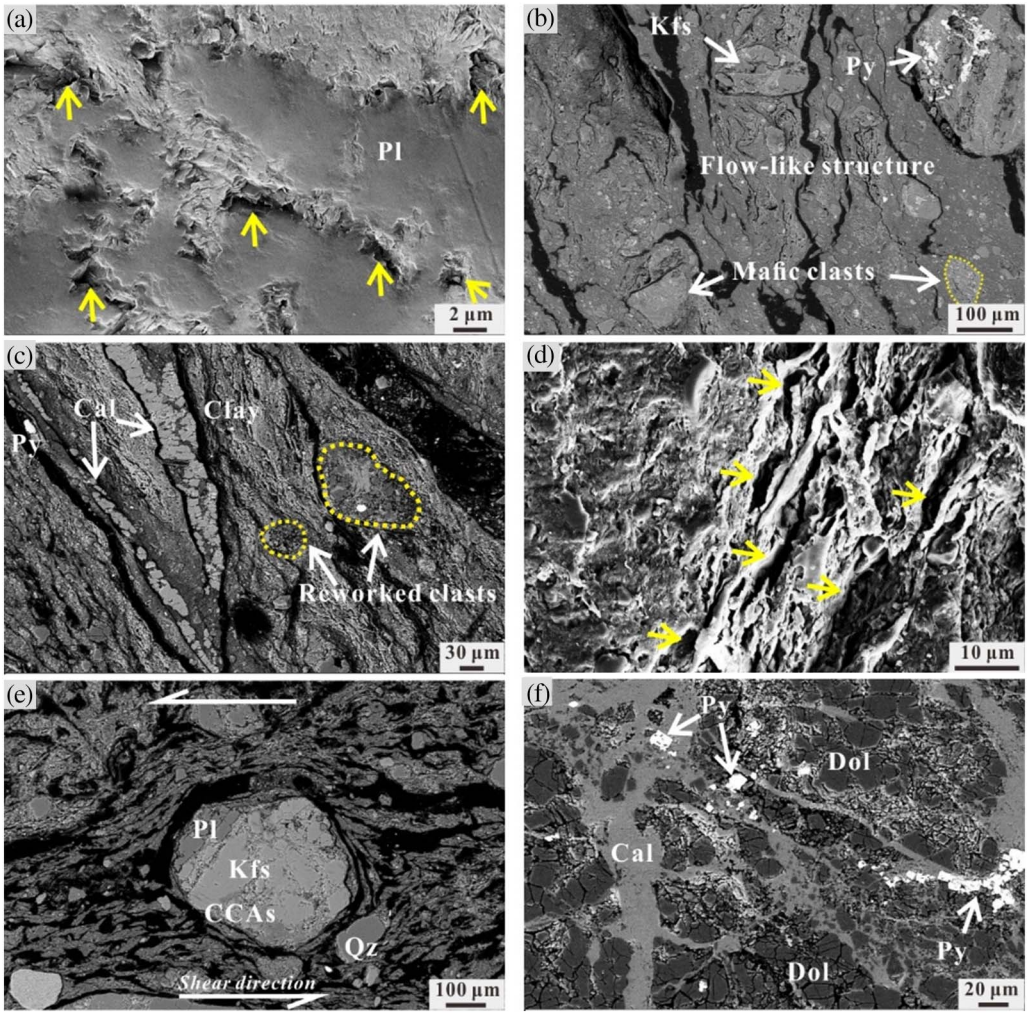

Fig. 5. Microstructures of typical fault rocks. Panel (a) is taken from the fine-grained granitic breccia, showing the matrix-supported framework and the development of micro-pores at the grain boundaries (indicated by yellow arrows). Panel (b) is from the yellow-green gouge, characterized by a flow-like structure and the widespread presence of reworked rock clasts. Panels (c–e) are from the black gouge, showing the presence of reworked clasts, calcite veins, pyrite, micro-pores, and clay-clast aggregates (CCAs), indicating strong fluid-rock interaction. (f) Footwall dolomitic cataclasite, with cracks filled with calcite veins and chains of pyrite. Annotations of minerals are as follows: Qz, quartz; Pl, plagioclase; Py, pyrite; Kfs, K-feldspar; Dol, dolomite; Cal, calcite. All the graphs were taken by a Zeiss ΣIGMA field-emission scanning electron microscope. (b), (c), (e) and (f) were taken under backscattered electron mode, and (a) and (d) were under secondary electron mode. (For interpretation of the references to color in this figure legend, the reader is referred to the web version of this article.)

V_2 in Fig. 7) were calibrated using a series of hard alloy cylinders with holes of various diameters. Porosity variations in response to each step change in confining pressure were determined from the induced pore pressure change with distilled water as the pore fluid, assuming that the entire volume variation represents the pore volume change in the specimen. Uncertainty for the initial porosity measurement is below 0.3% (Chen et al., 2013c). For the porosity change measurement, the uncertainty in the pore volume change during each step change in confining pressure is about 0.5 mm^3 (Chen et al., 2013c), which corresponding to an uncertainty of 0.16% in porosity for a sample with 10% porosity and with diameter of 20 mm and length of 10 mm.

In a typical experiment, a sample together with the upper and lower spacers was placed in a rubber jacket (Fig. 7). This whole sample assembly was inserted into the pressure vessel and then connected to the upstream and downstream pore pressure reservoirs. In a conventional test, the procedure for fluid transport properties measurement adopted is:

(1) Load the confining pressure to 10 MPa and evacuate the pore fluid pipelines. Then measure the initial porosity with nitrogen gas.
(2) Evacuate the pipelines again and introduce distilled water to saturate the flow lines and sample. Synchronously increase the confining pressure to 25 MPa and pore fluid pressure to 15 MPa.
(3) Measure the permeability and specific storage using the PPO method.
(4) Change the confining pressure and record the induced pore pressure variation to calculate the porosity change.
(5) Repeat steps (3) and (4) at each step change of confining pressure.

In such a procedure with confining pressure changing (both loading and unloading) between 25 MPa and 180 MPa, a full set of hydraulic property data of a sample, including the permeability, porosity, and specific storage can be obtained. This pressure range corresponds to depths of 0.6 to 10 km under subsurface assuming hydrostatic and lithostatic pressure gradients, and average crustal rock density of 2.65 g/cm^3.

5. Experimental results

5.1. Mineralogical results

XRD analysis results are presented in Fig. 8 and Table 2. The granitic host rock consists mainly of quartz and feldspar, and the fault rocks derived from it are composed primarily of quartz, feldspars, clays and calcite. Dolomite and calcite are the major minerals for the footwall carbonate-related rocks. As approaching the fault core (gouge zones), the feldspar and quartz contents show a remarkable decrease, whereas the total clay content behaves the opposite way, with a peak value of 65% achieved for the YGG (D3s-16-2). Calcite is enriched in the gouges compared to the hanging wall granitic rocks and footwall dolomitic rocks. In addition, a minor amount of pyrite occasionally appears in the fault core (Figs. 5 and 8).

The clay fractions of granitic fault rocks are identified to comprise of chlorite, illite, smectite, and kaolinite (Fig. 8). Clay assemblages of the

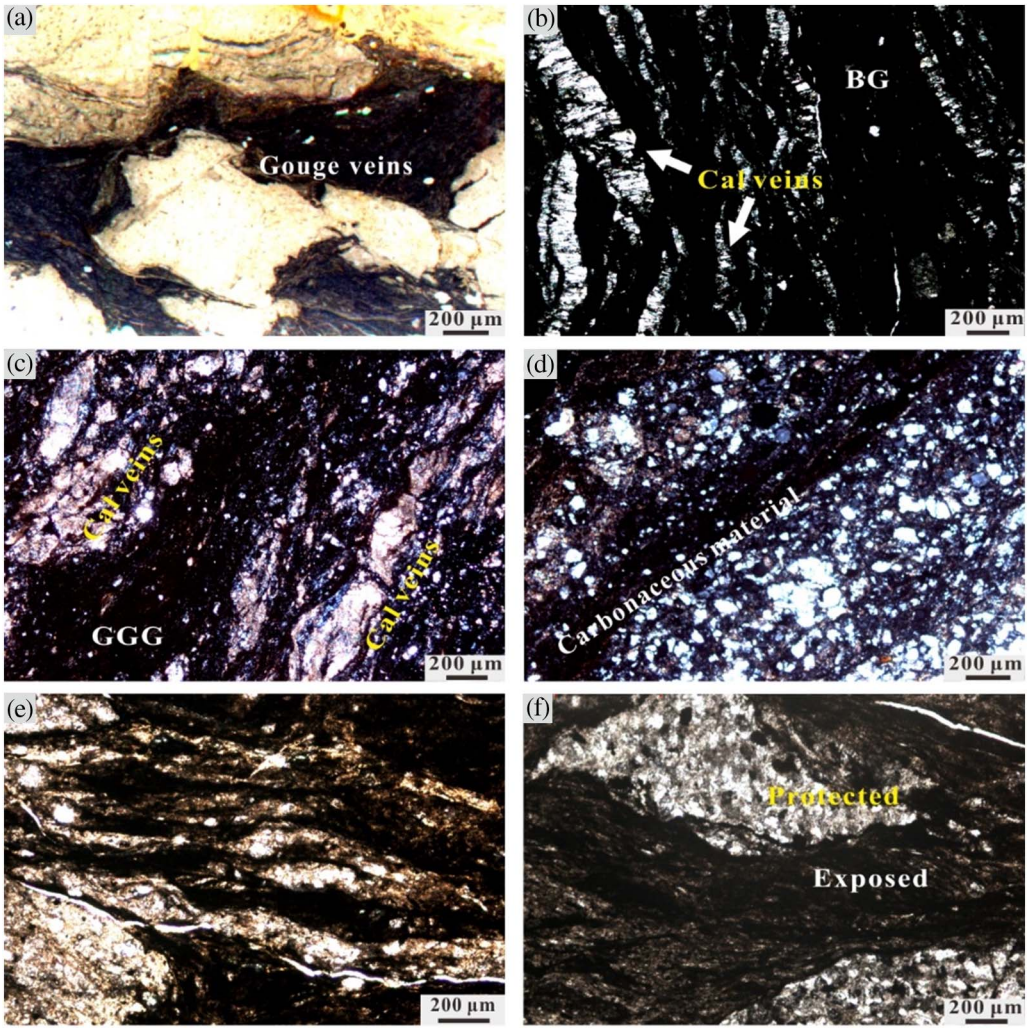

Fig. 6. Microstructural evidences indicate the presence of pressurized pore fluid and the associated healing process. (a) Black gouge veins injected into fractures in cataclasite. (b–c) Spar calcite vein precipitated in the black gouge and grey-green gouge. (d) Localized shear band in the cemented cataclasite, which is, of ~2 mm in thickness and enriched in carbonaceous material. (e) Pressure solution seams observed in the black gouge and cataclasite. (f) Pressure solution induced grain size reduction from protected to exposed area. BG, black gouge; GGG, grey-green gouge. (b), (c), (d), and (f) are optical images under crossed polarized light; (a) and (e) are under plane polarized light. (For interpretation of the references to color in this figure legend, the reader is referred to the web version of this article.)

YGG and GGG are composed mainly of chlorite, smectite, kaolinite and minor illite, and that of the BG are smectite, chlorite, and illite (Fig. 8, Table 2). The mineralogical data presented here are consistent with Duan et al. (2016), in which rather detailed mineralogical results have been reported.

5.2. Fluid transport properties

Integrated measurements of permeability, porosity, and specific storage were performed on 22 samples collected from the drilling cores and the surface outcrop. Experimental results, including permeability, porosity, and specific storage are presented against the changes in Terzaghi effective pressure ($P_e = P_c - P_p$, where P_e, P_c, and P_p are effective, confining and pore pressures, respectively) along the pressurization and depressurization paths (Figs. 9, 10, 11). The sample information and the key results are listed in Table 1.

5.2.1. Permeability

The permeability curves show a rapid decrease as P_e increases to about 65 MPa, followed by a gentler decrease as P_e increases from 85 MPa to 165 MPa (Fig. 9). Along the depressurization path, the permeability curves generally show a slight increase as P_e decreases from 165 MPa to 10 MPa. Permeabilities of the rock samples measured vary by up to 5 orders of magnitude within the P_e range investigated. The host rocks and gouges have the lowest permeability values, which lie between 10^{-18} m^2 and 10^{-22} m^2 (Fig. 9a, e). The mafic rock sample (D3s-16) shows an ultra-low permeable character, with a permeability value of 4.3×10^{-22} m^2 at P_e of 10 MPa, which is close to the detection limit of our experimental configuration. Under P_e of 165 MPa, permeabilities of fault gouge samples range from 2.6×10^{-21} m^2 to 2.1×10^{-22} m^2, with the lowest value being measured by the BG (D3s-31). Under a given P_e condition, permeabilities of the greenish gouges are ~1–2 orders of magnitude higher than the black gouges (Fig. 9e). Permeabilities of the granitic cataclasites range from 10^{-18} m^2 to 10^{-21} m^2 as P_e changing between 10 MPa and 165 MPa (Fig. 9b, c). Among them, permeability results of the mesh-fractured cataclasites (Fig. 9c) are generally higher than the cemented cataclasites (Fig. 9b). The granitic breccia samples show large permeability variations within a range of 10^{-18} m^2–10^{-22} m^2 (Fig. 9d). Consistent with the mesh-fractured cataclasites, the coarse breccia sample is also relatively permeable. However, the fine-grained breccia samples have relatively low permeabilities (Fig. 9d), which can be as low as 2.9×10^{-21} m^2 at 165 MPa P_e. Large permeability variations have also been observed in the footwall carbonate rocks (Fig. 9f and g). The mesh-fractured dolomitic cataclasites have relatively high permeabilities, which can be as high as 4.6×10^{-17} m^2. The footwall muddy limestone cataclasite, which is cemented by calcite veins (Fig. 4f) shows a relatively low permeable character, especially at high P_e, which can be as low as 3.2×10^{-21} m^2 at 165 MPa (Fig. 9g).

A fitting method is usually employed to describe how the hydraulic properties evolve with changes in pressure or increasing depth. Both exponential law (David et al., 1994) and power law (Shi and Wang, 1986) have been widely used to fit laboratory measured permeability data as a function of effective pressure. However, neither one can fit our

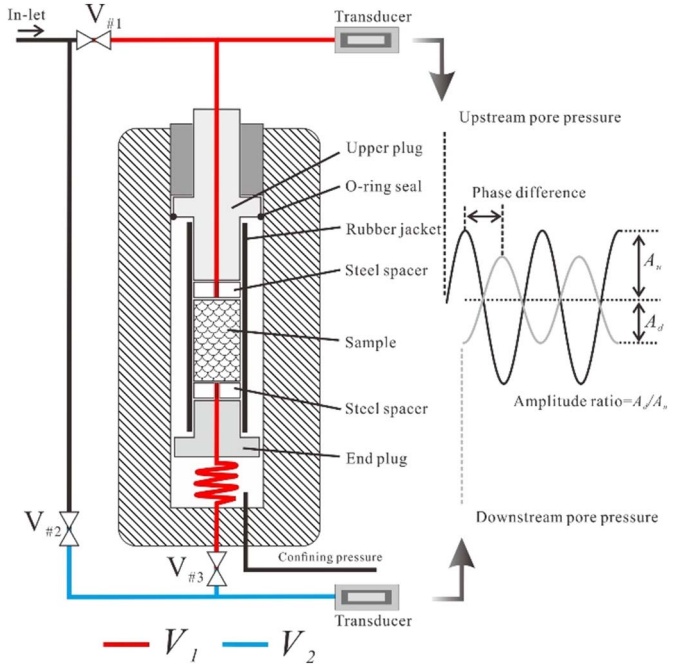

Fig. 7. Schematic configuration of the hydraulic property measurement system used in the present experiments. In each experiment, the sample assembly with the end plugs was placed inside the pressure vessel, then connected to the upstream and downstream reservoirs, and loaded to the designed confining pressure conditions. A pressure signal of sinusoidal oscillation was imposed at the upstream end of the sample, and the response at the downstream end was recorded. Comparison of the two signals allows for the permeability and storage measurements using the pore pressure oscillation method (see Chen et al., 2015 of this system for details).

data very well in the whole P_e range because the permeability curves usually show a rapid reduction with the initial increase of effective pressure but followed by very slight permeability decrease during the following pressurized steps (Fig. 9). Therefore, to fit the data more precisely, we performed sectional curve fitting in the P_e ranges of 10–65 MPa and 85–165 MPa, respectively. The decrease in permeability with increasing P_e is described as an exponential relation $k = k_0\exp(-\gamma(P_e - P_0))$, where k is permeability, k_0 is the permeability at a reference pressure (P_0), and γ is the corresponding pressure sensitivity (e.g., Rice, 1992; David et al., 1994). In the two pressure ranges (10–65 MPa and 85–165 MPa), P_0 was set as 10 MPa and 85 MPa, respectively. Fitting results are presented in Table 1. The γ values from the low P_e interval are commonly lower than those from the high P_e interval. In the low P_e interval, γ values of the fault gouge and host rock samples are mostly range between 0.03 MPa^{-1} and 0.08 MPa^{-1}, but those of the coarse breccia and cataclasite samples are range between 0.01 MPa^{-1} and 0.04 MPa^{-1}. In the high P_e interval, γ values generally range between 0.002 MPa^{-1} and 0.03 MPa^{-1}. Regarding the pressure sensitivity, the fault gouge and host rock samples are the most sensitive, reducing the permeability by almost three orders of magnitude as P_e increases from 10 MPa to 165 MPa. The coarse breccia and cataclasite samples are less sensitive, permeability reductions of these samples as P_e increases from 10 MPa to 165 MPa are mostly smaller than one order of magnitude (Fig. 9b, c, d and f).

5.2.2. Porosity

The results of porosity are presented in Fig. 10. The initial porosities (measured at P_e of ~10 MPa) mostly fall between 1% and 21%, except the host rocks and cemented cataclasites whose porosities are too low to measure using the present method. Different kinds of fault rocks are well featured by their variations in porosities. Porosities of the fine-grained breccia samples are predominately range between 8.9% and

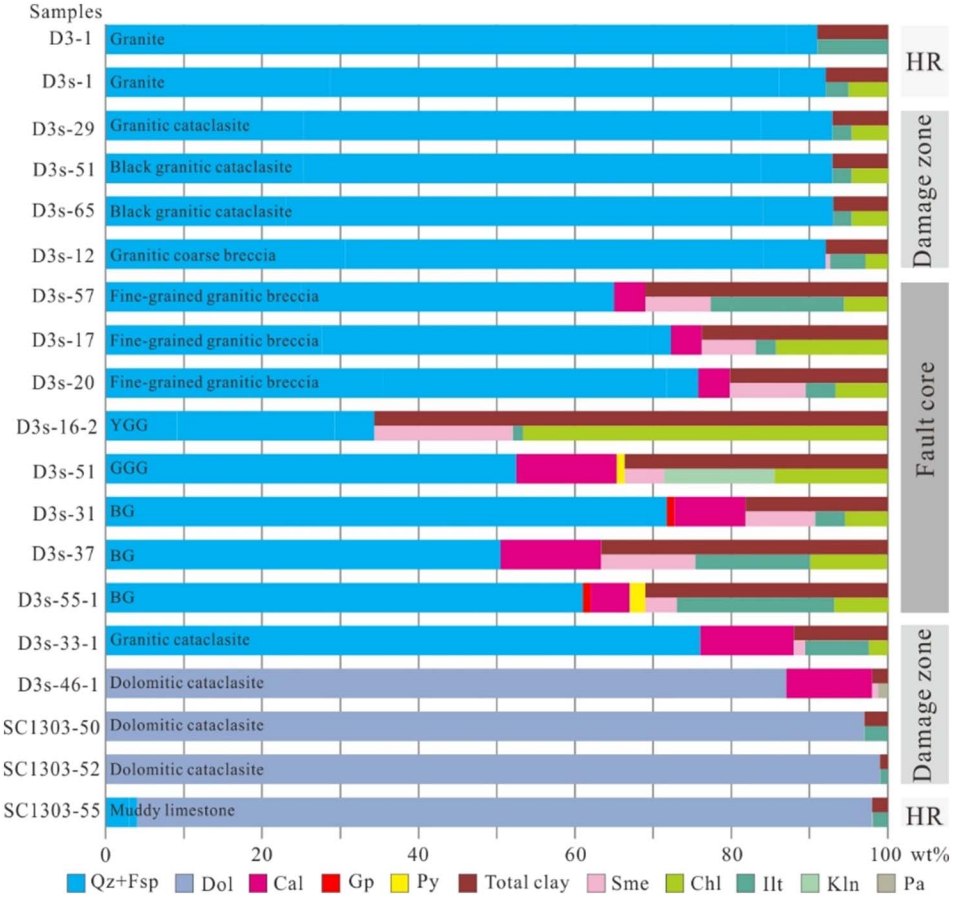

Fig. 8. Mineral assemblages of the experimental samples. The abbreviations HR, YGG, GGG, and BG represent host rock, yellow-green gouge, grey-green gouge, and black gouge, respectively. Annotations of minerals are as follows: Qz, quartz; Fsp, feldspar; Gp, gypsum; Cal, calcite; Py, pyrite; Dol, dolomite; Sme, smectite; Chl, chlorite; Ilt, illite; Kln, kaolinite; Pa, palygorskite. (For interpretation of the references to color in this figure legend, the reader is referred to the web version of this article.)

Table 2
Mineral compositions of selected samples.

Sample no.	Bulk composition								Clay composition (ref.%)				
	Qz	Pl	Kfs	Gy	Cal	Py	Dol	Clay	Sme	Ilt	Kln	Chl	Pa
D3-1	41%	46%	4%	–	–	–	–	9%	–	100	–	–	–
D3-29	25%	58%	9%	–	–	–	–	7%	–	35	–	65	–
D3-65	23%	61%	9%	–	–	–	–	7%	–	34	–	66	–
D3s-1	29%	58%	6%	–	–	–	–	8%	–	37	–	63	–
D3s-12	31%	54%	8%	–	–	–	–	8%	7	57	–	36	–
D3s-16-2	9%	20%	5%	–	–	–	–	65%	27	2	–	71	–
D3s-17	28%	42%	3%	–	4%	–	–	24%	29	11	–	60	–
D3s-20	35%	36%	4%	–	4%	–	–	20%	48	19	–	33	–
D3s-31	43%	25%	3%	1%	9%	–	–	18%	49	21	–	30	–
D3s-33-1	76%	–	–	–	12%	–	–	12%	12	68	–	20	–
D3s-37	51%	–	–	–	13%	–	–	37%	33	40	–	27	–
D3s-46-1	–	–	–	–	11%	–	87%	2%	36	3	–	–	61
D3s-51	14%	39%	–	–	13%	1%	–	34%	15	–	42	43	–
D3s-55-1	61%	–	–	1%	5%	2%	–	31%	13	65	–	22	–
D3s-57	25%	40%	–	–	4%	–	–	31%	27	55	–	18	–
SC1303-50	–	–	–	–	–	–	97%	3%	–	100	–	–	–
SC1303-52	–	–	–	–	–	–	99%	1%	3	97	–	–	–
SC1303-55	3%	–	1%	–	94%	–	–	2%	3	96	–	1	–

Qz, quartz; Pl, plagioclase; Kfs, K-feldspar; Gy, gypsum; Cal, calcite; Py, pyrite; Dol, dolomite; Clay, total clay; Sme, smectite; Ilt, illite; Kln, kaolinite; Chl, chlorite; Pa, palygorskite; "–", denotes content below detection.

17.2% as P_e changing between 10 MPa and 165 MPa; while those of the cataclasite and coarse breccia samples are generally lower than 5% (Fig. 10a, b). Notwithstanding having low permeability values, the gouge samples have relatively higher porosities (10.5%–21.0%). Again, porosity results of the gouge samples show a rapid reduction as P_e increases (Fig. 10c), and similar trends are observed for the granitic fault breccias (Fig. 10b), except the D3s-12 sample that has extremely coarse grain size. A variation of porosity has also been observed in the footwall carbonate rocks (Fig. 10d). Porosities of the cataclasites and footwall carbonate rocks show a very slight decrease as P_e increases. Similar to permeability, the depressurize curves of porosity show much gentler trends, indicating smaller sensitivities as the depressurization paths.

5.2.3. Specific storage

Specific storage is defined, at a given fluid density, as the volume change of pore fluid stored in a unit volume sample due to a unit pore pressure change. It has been previously proved that specific storage results measured by the PPO method might suffer uncertainties because the measuring system usually has a much larger downstream storage than the samples themselves (Fischer and Paterson, 1992; Bernabé et al., 2006). In this study, uncertainty analyses on specific storage results following the method given by Bernabé et al. (2006) testify to a high confidence level except for the host rocks and some cemented cataclasite samples, whose specific storages are below the detection limit ($\sim 10^{-12}$ Pa^{-1} for our experimental configuration with the PPO method). The consensus finding is that porosities of these samples are also below the detection limit or fall in an ultra-low level (below 2% at the initial P_e of 10 MPa).

As shown in Fig. 11, the specific storage results exhibit rapid reduction curves as P_e increases. The specific storages of the cataclasite sample and most breccia samples predominately range from 10^{-11} Pa^{-1} to 10^{-12} Pa^{-1} (Fig. 11a), and those of the gouge samples are slightly higher (range from 10^{-10} Pa^{-1} to 10^{-11} Pa^{-1}), especially at lower pressures, which can be as high as 3.4×10^{-10} Pa^{-1} (Fig. 11b). Again, the specific storages show a decrease with increasing effective pressure and vice versa. The coarse breccia sample (D3s-12) shows the highest sensitivity to the pressure change, and its value drops to 4.3×10^{-12} Pa^{-1} under the maximum P_e (Fig. 11a).

6. Discussion

6.1. Hydrological features of the YBF

Hydrological structure of the YBF at the GR, represented by the variations of different hydraulic properties against the distance from the PSZ, is shown in Fig. 12. The results show that at a given effective pressure (e.g., 165 MPa), the host rocks and the mafic rock in the hanging wall have the lowest permeabilities (generally below 6.0×10^{-21} m^2), which are followed by the fault gouges and fine-grained fault breccias taken from the fault core (between 6.9×10^{-21} m^2 and 2.1×10^{-22} m^2). The mesh-fractured cataclasites and the coarse fault breccias derived from the damage zones show the highest permeabilities, which are larger than 5.0×10^{-21} m^2 at P_e of 165 MPa. The footwall host rocks that are represented by the well-cemented muddy limestones also exhibit low permeabilities (3.2×10^{-21} m^2 at P_e of 165 MPa). Permeability profiles at different pressures (10 MPa and 165 MPa) show similar trends (Fig. 12a), suggesting that the YBF at the GR outcrop has a typical "conduit/barrier" hydraulic structure (Caine et al., 1996), with the low permeable host rocks and fault core acting as barriers, and high permeable damage zones acting as fluid conduits. The impermeable fault core has a stable thickness of 3.3 m, and those of the hanging wall and footwall damage zones are 10 m and 63 m, respectively. These results display a spatial macroscopic anisotropy in permeability across the fault, which favoring fluid flow in the high permeable damage zones and the low permeable fault core may prevent fluids from flowing across it. Similar structure has been previously observed at other exposures along the YBF (the Zhaojiagou (Chen et al., 2013a), Pingxi (Chen et al., 2013c), and Bajiaomiao (Chen et al., 2016) outcrops, Fig. 1), indicating a consistent hydraulic structure along the length of the YBF. Our results are also in agreement with the permeability structure on other major active fault zones, such as the Nojima fault (Lockner et al., 2000; Mizoguchi et al., 2008), the Chelungpu fault (Tanikawa and Shimamoto, 2009), the San Andreas fault (Morrow et al., 2014), and the Alpine fault (Boulton et al., 2012; Carpenter et al., 2014).

Despite the broad consistency, the GR outcrop has the following distinct features. First, the surface rupture of the YBF cuts into either the clastic sedimentary or carbonate rocks at the locations reported in previous studies. While at the GR outcrop, the host rocks are complex (Fig. 1, site 4), with the principal slip surface associated with the

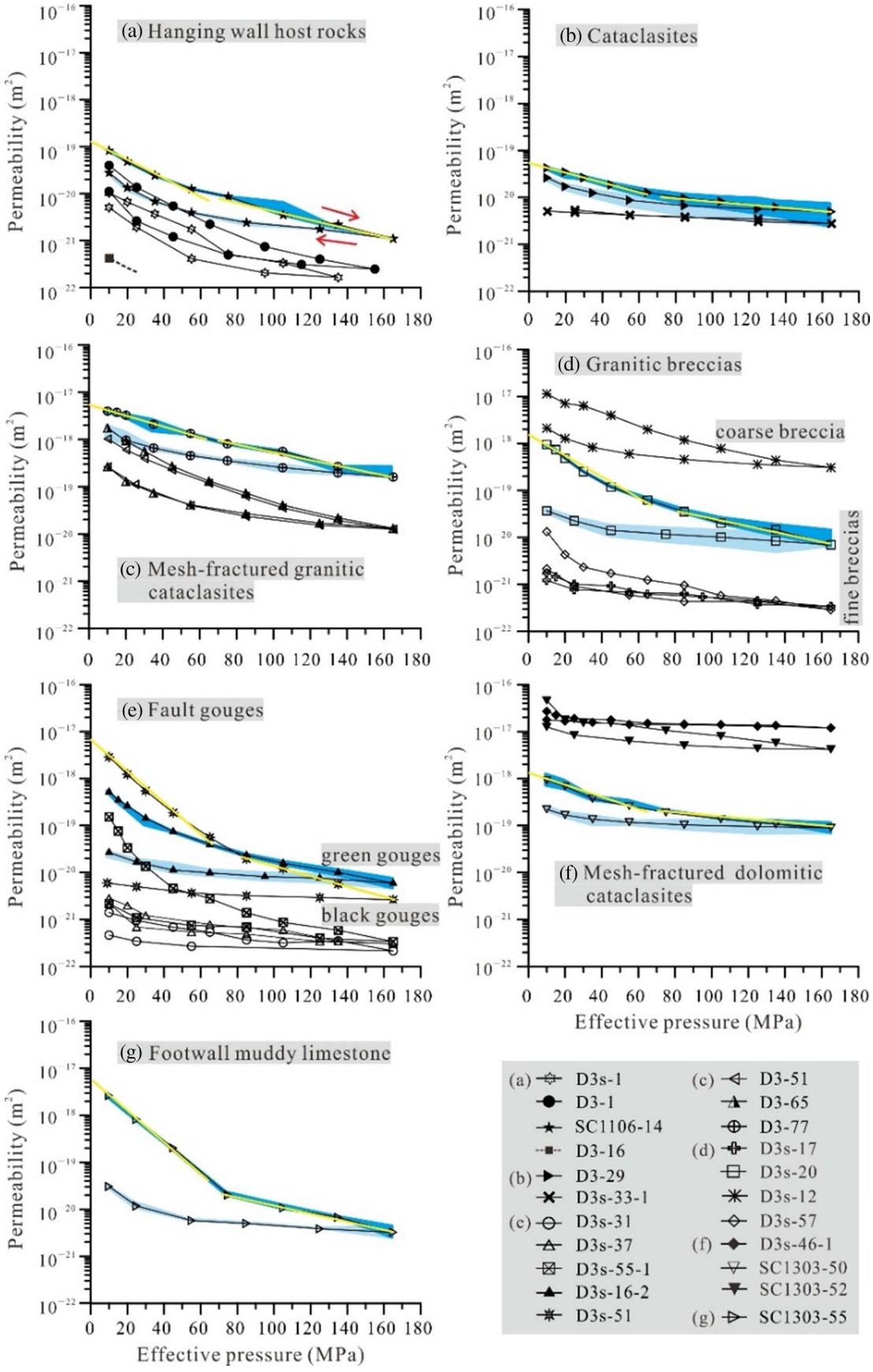

(caption on next page)

Fig. 9. Permeability results as a function of effective pressure. (a) Results of the hanging wall host rocks. (b–c) Results of the cataclasites and mesh-fractured cataclasites. (d–e) Results of the fault breccias and fault gouges. (f–g) Results of the footwall carbonate cataclasites. Red arrows in (a) indicate the upward and downward pressurization paths. For all samples, permeability results from the downward pressurization paths are generally lower than the results from the upward paths. The yellow lines denote the exponential regression fitting lines of permeability in the effective pressure ranges of 10–65 MPa and 85–165 MPa, respectively. The blue shaded areas indicate the uncertainties of permeability for the oscillating pore pressure method. Only example data of uncertainties and fitting curves are shown here. Detailed fitting results are listed in Table 1. (For interpretation of the references to color in this figure legend, the reader is referred to the web version of this article.)

Wenchuan earthquake being inferred to cut through the granitic rocks (Duan et al., 2016). Second, the rupture zone at the GR outcrop is > 100 m in width, much larger than those observed at the Pingxi and Zhaojiagou outcrops, which are < 10 m in width (Chen et al., 2013a; Yao et al., 2013). Third, extremely low permeabilities were measured for the fault gouges at the GR site, especially for the BG layer, which has permeabilities of 1.4×10^{-19}–2.1×10^{-22} m^2 at P_e of 10–165 MPa (Fig. 9e), much lower than the gouges collected from the Zhaojiagou and Pingxi outcrops that have permeabilities of 10^{-18}–10^{-21} m^2. Additionally, permeability of the BG is also significantly lower than the gouges from other major active fault zones, such as the Chelungpu fault zone (10^{-16}–10^{-19} m^2 at P_e of 60 or 180 MPa, Tanikawa et al., 2009; Tanikawa and Shimamoto, 2009), the Nojima fault zone (10^{-18}–10^{-20} m^2 at P_e of 180 MPa, Mizoguchi et al., 2008), and the Alpine fault zone (10^{-19}–10^{-20} m^2 at P_e of 30 or 63 MPa, Boulton et al., 2012; Carpenter et al., 2014). Our recent study has shown that the BG, which has accommodated significant displacement in multiple increments of shear, shows high degree of fracturing, grain comminution, and fluid-rock interactions (Duan et al., 2016). We propose that the enrichment of clay minerals and re-precipitated vein materials (e.g., calcite, pyrite) lead to the essentially low permeable nature of the fault gouges. Finally, the GR outcrop develops a > 2 m thick continuous gouge zone, which is obviously thicker than other sites of the YBF (e.g., several centimeters to tens of centimeters thick, Chen et al., 2013b, Yao et al., 2013) and other typical fault zones (e.g., Caine et al., 1996). In view of the low permeability, such thick gouge zone could efficiently work as an impermeable fluid barrier (see detailed discussion in Section 6.3.1). It is also noteworthy that the pore fluids (usually gas or water) that used for experiment may also contribute to the permeability discrepancy. Most of the previous permeabilities were measured using gas as the pore fluid (e.g., Mizoguchi et al., 2008; Tanikawa et al., 2009; Chen et al., 2011), whereas water was used in the present study. Recent

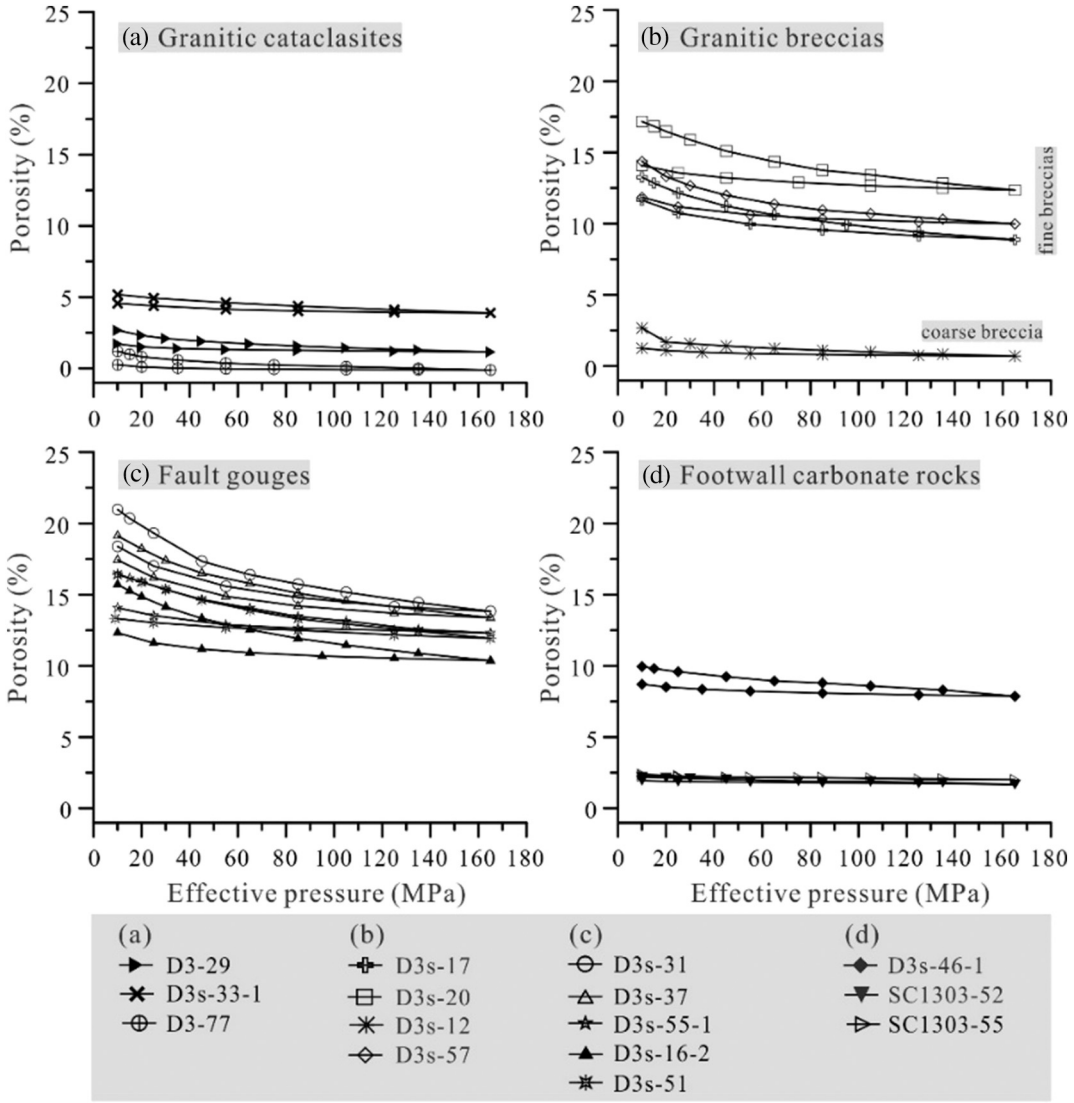

Fig. 10. Porosity results as a function of effective pressure. (a) Results of the granitic cataclasites. (b–c) Results of the fault breccias and fault gouges. (d) Results of the footwall carbonate rocks.

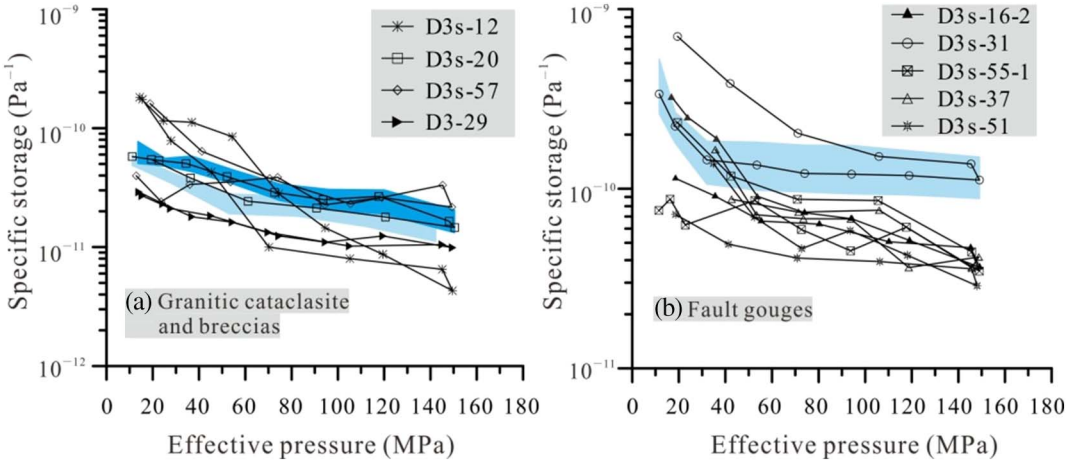

Fig. 11. Specific storage results as a function of effective pressure. (a) Results of the granitic cataclasite and breccias. (b) Results of the fault gouges. The blue shaded areas indicate the uncertainties of specific storage for the oscillating pore pressure method. (For interpretation of the references to color in this figure legend, the reader is referred to the web version of this article.)

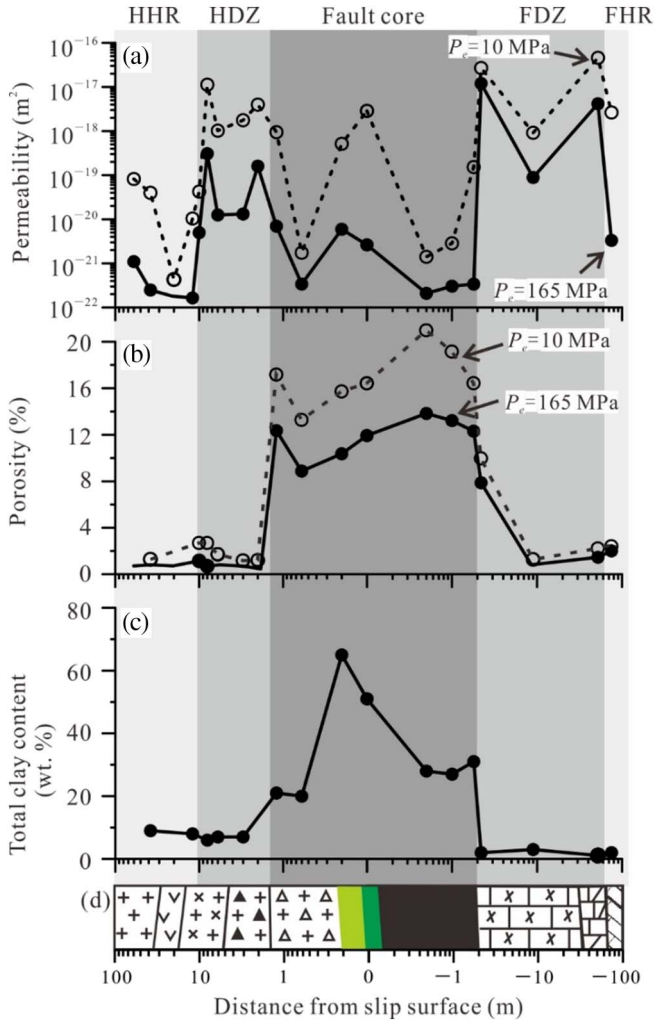

Fig. 12. Profiles of permeability (a), porosity (b), and clay content (c) plotted as a function of the logarithmic distance from the slip surface across the Golden River outcrop. Lithological symbols of the transverse section are as fig. 3. The open and solid circles are results at 10 MPa and 165 MPa effective pressures, respectively. HHR, hanging wall host rock; HDZ, hanging wall damage zone; FDZ, footwall damage zone; FHR, footwall host rock.

studies showed that gas permeability of fault rocks could be much higher than the permeability to water, in particular for the fault gouges, due to the hydrophilic and swelling properties of the constitutive clay minerals (Faulkner and Rutter, 2000; Behnsen and Faulkner, 2011; Duan and Yang, 2014).

In this study, the hanging wall and fault core samples were collected from the drill cores; the footwall samples were collected from the surface outcrop. Weathering products may fill in cracks and pores of surface rocks and probably make these samples more permeable and insensitive to confining pressure (Morrow and Lockner, 1994). Our microscopic observations show that the footwall samples have suffered strong damage and fluid-rock interactions, with a few weathering products. Other laboratory studies on fault rocks collected from surface outcrops, such as the Nojima fault (Mizoguchi et al., 2008) show no significant permeability difference with drill core samples from the same gouge zone (Lockner et al., 2000). Based on the tidal response of water level in the first borehole of the Wenchuan Earthquake Fault Scientific Drilling (WFSD-1), Xue et al. (2013) tracked the in-situ damage zone permeability in the depths of 800 to 1200 m, which corresponding to effective pressures of 13.2 to 19.8 MPa assuming lithostatic and hydrostatic pressure gradients. The average permeability was estimated to be $\sim 1.4 \times 10^{-15}$ m^2, which is 1–2 orders of magnitude higher than the upper bound of our laboratory measurements, i.e., 5.0×10^{-17} m^2 at 10 MPa effective pressure (Fig. 9). A similar discrepancy between the laboratory-derived and in-situ measured permeabilities has also been found in the Nojima fault (e.g., Kitagawa et al., 2002; Mizoguchi et al., 2008) and in the Nankai accretionary prism fault (Boutt et al., 2012). This might be explained by the scale effect because fluid flows in laboratory core-scale cracks are not always representative of large-scale flows in fractures and joints in the field (Boutt et al., 2012; Mitchell and Faulkner, 2012). The laboratory-derived permeabilities presented in this study may be appropriate for representing in-situ values for the fault core, and probably for the lower bound (i.e., matrix permeability) of the damage zones (Morrow et al., 2014).

The variations of porosity are not always consistent with the permeability trends addressed above. Although the fault core samples (i.e., fault gouges and fine-grained fault breccias), for instance, have very low permeabilities, their porosities and specific storages are relatively high (Fig. 13). Similar results have been observed previously in other fault zones (e.g., Tanikawa et al., 2009). As shown in Fig. 12b, host rock samples have the lowest porosities ($< 2\%$, most of them are too low to measure using the present method), which is tightly followed by the cataclasites (1%–3% at P_e of 10 MPa). The fine-grained breccias and fault gouges taken from the fault core own the highest porosities, which

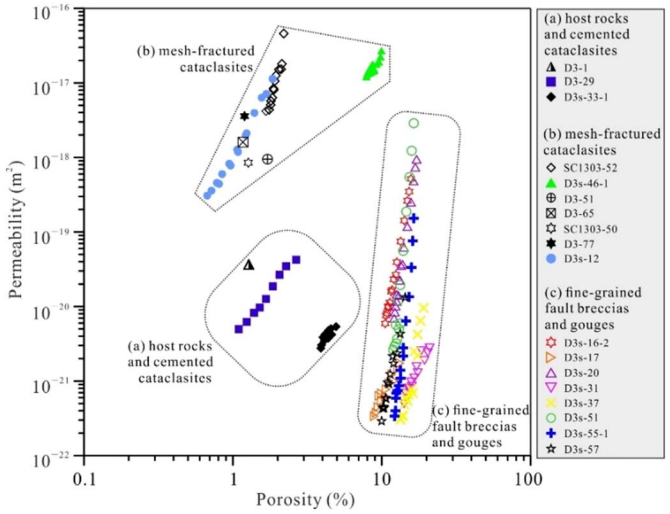

Fig. 13. Cross-plot between permeability and porosity. The data points of each kind of samples concentrate in different areas. The host rocks and cemented cataclasites have consistently low permeability and low porosity (a). The mesh-fractured cataclasites have low porosity but relatively high permeability (b). The gouges are characterized by high porosity but relatively low permeability (c).

are 13%–21% at 10 MPa, and declining to 8.8%–13.8% as P_e increases to 165 MPa. The same trends apply for the specific storages (Fig. 11). We propose that behaving as the fluid barrier, the high porosity fault core, works as the main area for the storage of fluid within the fault zone. This is supported by our microscopic observations that the fault gouges and fine-grained breccia samples contain a lot of micro-pores (Fig. 5a, d). High porosity and high specific storage of the fault core samples also imply that fluid trapped could be easily pressurized, generating excess pore pressure, as will be discussed in Section 6.3.

6.2. The fluid conduction and sealing mechanisms

Macroscopic and microscopic observations of the samples (i.e., host rocks, cataclasites, fault breccias, and fault gouges) indicate that the cohesive and incohesive rocks have different kinds of pores and cracks that constitute fluid pathways and dominate fluid flow. The cohesive samples, which commonly have low porosities ($< 5\%$ at P_e of 10 MPa, Table 1, Fig. 10), fall into three types according to their crack distribution and hydraulic conduction features (Fig. 4). The intact host rocks have the lowest permeabilities (as low as 4.3×10^{-22} m^2 at P_e of 10 MPa), which are tightly followed by the well-cemented cataclasites (from 5.8×10^{-21} m^2 to 4.3×10^{-20} m^2 at P_e of 10 MPa), while mesh-fractured cataclasites have the highest permeabilities (as high as 4.6×10^{-17} m^2 at P_e of 10 MPa). Microscopic observations indicate fluid migration in the mesh-fractured cataclasites are generally through the (micro)-cracks contained in the samples (Figs. 4 and 6). Moreover, the cohesive samples have relatively low γ-values (from 0.01 MPa^{-1} to 0.04 MPa^{-1}, Table 1), implying a low sensitivity of crack permeation to the changes in pressure. In contrast, the incohesive samples, characterized by higher porosities (13.3%–21.0% at 10 MPa), show a significant variation of permeability, depending on their distinct fluid conduction pathway. In particular, the fine-grained fault breccias and fault gouges, which have extremely low permeabilities (as low as 2.1×10^{-22} m^2 at P_e of 165 MPa), are featured by small grain sizes and abundant clay minerals (Figs. 5 and 8). Our XRD analyses revealed that the fault core (consisting of crushed fault breccias and fault gouges) shows an increase in clay content toward the (principal) slip zone, consistent with the variation of permeability (Fig. 12). Microscopic observation showed a matrix-supported framework and the presence of large amount of micro-pores within the framework, which are inferred to be the main fluid conduction pathways (e.g., Fig. 5a, d). Moreover, high γ-values imply that compaction operates more efficiently in the incohesive rocks, which is presumably due to the low frictional strength of the clay minerals therein (e.g., Zhu et al., 1997; Bernabé et al., 2004; Takahashi et al., 2007; Behnsen and Faulkner, 2011). Under water-saturated condition, clay minerals have considerably lower frictional strength than dry sample. Particles in such samples can move more easily and cause the rearrangement of the pore fabric during compaction (Behnsen and Faulkner, 2011). On the contrary, the coarse breccia samples have smaller clay content and larger grain size, showing a typical clast-supported structure. The higher permeability observed is attributed to the fluid conduction through network cracks and micropores, as widely observed in these samples.

Recently, rapid post-seismic recovery of the in-situ permeability of the YBF was revealed by Xue et al. (2013) using the fluctuation of water levels in the WFSD-1 borehole. Although our permeability measurements cannot provide direct evidence for such healing process, the results indeed show that the permeabilities of different types of (fault) rocks vary with their cementation structure (Fig. 4). Our composition analyses also indicate that the fault zone studied has undergone widespread fluid-related sealing process. The observed healing and sealing processes in the samples do not represent the post-process after the Wenchuan earthquake, but such observations reflect the complex healing process during the long-term active history of the LFZ. First, calcite veins are the most common cementation materials. They are widely found in the gouges (Figs. 5c and 6b, c), dolomitic cataclasites (Fig. 5f) and muddy limestone (Fig. 4f). Other minor minerals found in the fault zone include pyrite (Fig. 5b, f) and gypsum (Fig. 8). Calcite generally presents in the form of mineral veins and always fills in the fractures of fault rocks. Similarly, pyrites in the fault rocks also commonly distribute along fractures and forming the pyrite chains (Fig. 5f). The occurrence and distribution of theses minerals consistently indicate that they were precipitated from mineral fluids. For the gypsum, we cannot determine whether it was precipitated from fluid or formed by the oxidation of pyrite (Pirlet et al., 2010), but both require the participation of fluids. The presence of these minerals indicates widespread fluid flow and mineral precipitation in the fault zone. Second, authigenic clay minerals (i.e., smectite, chlorite, illite) are found to be widely present in the GR fault zone, especially in the fault core (Fig. 8, Table 2). Although clay minerals are not usually present as infilling vein material in cracks, they are important in sealing the incohesive fault rocks, such as the fine-grained breccias (Fig. 5a) and fault gouges (Fig. 5c, d). Third, carbonaceous materials are found to be present in the black cataclasites and BG, usually distributing along the cracks (Fig. 4g, h and i) and localized shear zone (Fig. 6d). Recent studies have revealed the widespread presence of carbon in several outcrops along the YBF (Togo et al., 2011; Kuo et al., 2014; Wang et al., 2014; Chen et al., 2016; Liu et al., 2016). Although the origin of carbonaceous materials in fault zones are poorly understood, their presence is presumably inferred to be related to fluid activities and involved in fluid-related healing and sealing processes (e.g., Liu et al., 2016; Kouketsu et al., 2017). Finally, pressure solution might be an important mechanism for healing and sealing of the fault rocks. Several pieces of microstructural evidence of pressure solution have been observed, such as the pressure solution seams (e.g., Fig. 6e) and grain size reduction (Fig. 6f). Stress promotes dissolution at grain contacts or cleavages, and removing the soluble species with insoluble materials forming the black seams. Enrichment of phyllosilicates and large volume loss in the GR fault zone (Duan et al., 2016) also indicate the widespread dissolution-precipitation. Though not that important at the shallow surface, pressure solution can become increasingly important at relatively deep depths (Gratier et al., 2003, 2011), especially during the long-term interseismic process.

The above discussions consistently indicate that a common physicochemical process might be responsible for the broad consistency between the hydraulic properties and internal structures of the fault rocks. We propose that mechanical cataclasis, which leads to cracking

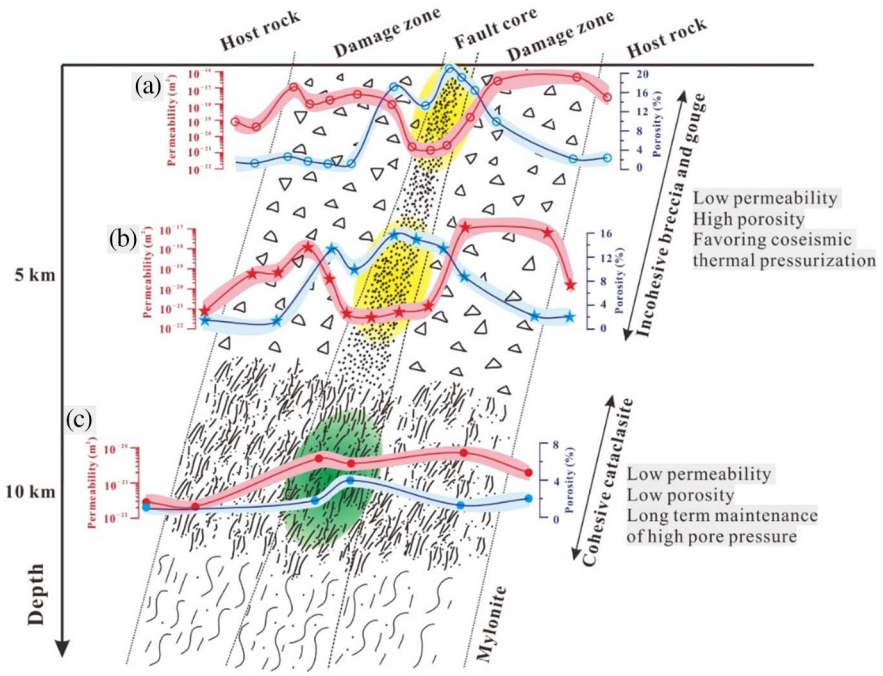

Fig. 14. Schematic diagram of fault profile showing the distribution of fault rocks and laboratory measured fluid transport properties. Fault rock distribution in the fault zone with depth is adopted from Sibson (1977). In applying our laboratory data to the subsurface, incohesive fault breccia and fault gouge can be typical rocks in the shallow fault zone (e.g., 5–7 km). Cohesive cataclasites are representative rocks at relatively deeper depths (e.g., 7–10 km). Panel (a) is permeability (red symbols) and porosity (blue symbols) data measured at 10 MPa effective pressure, corresponding to about 600 m depth at the shallow subsurface. Panel (b) is permeability and porosity data measured at 85 MPa effective pressure, corresponding to about 5 km depth. Panel (c) is permeability and porosity data measured at 165 MPa effective pressure, corresponding to about 10 km depth. (For interpretation of the references to color in this figure legend, the reader is referred to the web version of this article.)

and grain size reduction, and fluid-rock interactions, which lead to clay formation, mineral precipitation and cementation/healing of the fault rocks, dominate the hydraulic properties and their responses to the fault zone evolution.

6.3. Low permeable fault and its implications

6.3.1. Implication for sealing high pore fluid pressure

According to Sibson's (1977) fault model and our laboratory data, we established a conceptual fault zone model illustrating the distribution of fault rocks and fluid transport properties at different depths (Fig. 14). In extrapolating our experimental data to the subsurface, the incohesive fault breccias and gouges can represent the shallow condition (e.g., < 5–7 km, Sibson, 1977), while the fracture-free, well-cemented cataclasites may be applied to relatively deeper depths (e.g., ~10 km, Sibson, 1977). The results show that the fault core has very low permeability but high porosity at the shallow portion (Fig. 14a, b). With increasing depths around ~10 km, the fault zone has low permeability and low porosity (Fig. 14c). In particular, considering the original formation depths (e.g., > 7 km, Scholz, 2002) and low permeability feature of the fracture-free cataclasites (< 4.3×10^{-20} m^2, Table 1, Fig. 9b, D3-29 and D3s-33-1), these samples may have recorded deformation inherited from past fault motions and healing processes associated with fluid-rock interactions, perhaps during the long-term exhumation history from the depths where cohesive cataclasites initially developed (Sibson, 1977; Woodcock and Mort, 2008). Although coseismic slips can create cracks and enhance permeability, cracks at such depths (~10 km) with high temperature and pressure can heal rapidly during the post-seismic processes. It is expected that low permeability is required in and around the fault zone to maintain the high pore pressure for rupture to nucleate at a mid-crustal depth (Sibson et al., 1988; Hickman et al., 1995). Previous mechanical analysis also indicated that a high pore pressure is necessary for the YBF to nucleate a large earthquake (Zhou and He, 2009). Several models have been proposed to depict the evolution of fluid pressure associated with seismic cycles such as continuous upwelling of fluids at depth (Sibson et al., 1988; Byerlee, 1990; Rice, 1992). In these models, rapid sealing of fault rocks is postulated to cause significant decrease in fault zone permeability. Low permeability is thus required in the fault zone to accumulate and maintain high pore fluid pressure for rupture nucleation at seismogenic depths (e.g., 6–18 km for the Wenchuan earthquake). This consideration is consistent with our measurement of low permeabilities for the cemented cataclasites at the seismogenic depths (Fig. 14c), supporting the possible maintenance of high pore pressure at depths.

However, our results also revealed quite high permeability for the mesh-fractured cataclasites and coarse breccia (Fig. 9). This discrepancy can be explained by the different deformation and healing histories that these rocks have experienced. Intensive grain size reduction and widespread presence of reworked clasts and crosscutting veins seen in the gouges indicate multiple increments of shear (Duan et al., 2016). Strong cataclasis and fluid-rock reactions in the fault gouge lead to grain size reduction, enrichment of clays and precipitation of veins, and thus low permeability. The fault breccias have suffered severe fracture damage during the Wenchuan earthquake. They were cored ~3 years after the quake, and thus more likely represent the hydrological properties of the fault zone in the post-seismic period (Xue et al., 2013). This time interval is not long enough for the damages newly formed in the cataclasites or coarse breccia to heal completely, as the healing processes involved are relatively slow. The fractured cataclasites with high permeability (> 1.0×10^{-18} m^2 at 10 MPa) may record damages along the exhumation history and from recent earthquakes, which result in the enhanced permeability. Previous study also showed that permeability of cataclasites could be significantly increased by fracture dilatancy created in laboratory experiments (Uehara and Shimamoto, 2004). Given that the damage zones have very high permeabilities (Fig. 14a, b), they may efficiently work as conduits for fluid flow and thus disadvantage for the long-term accumulation of high pore pressure in the shallow fault zone (e.g., Rice, 1992).

The gouge zone at the GR outcrop has a stable thickness of 2 m and extends stably on the surface (Fig. 3). This gouge zone can be observed at the borehole depth (Fig. 3) and can also found on the mountaintop (~30 m high) of the outcrop (Fig. 3a), extending for totaling 75 m along the dip direction. As shown in Fig. 14a and b, extrapolation of the fluid transport properties of the gouge samples to the shallow fault zone reveals a low permeability but high porosity character in the fault core. In particular, the gouge samples, consisting of fine-grained materials and a large percentage of phyllosilicates, have a typical matrix-supported structure and very low permeability. This kind of structure could strongly restrain the fluid transport efficiency with increasing confining

pressure. Such hydraulic properties imply that the fault core is a potential area for the storage of fluids, and the low permeability could significantly prevent frictional heated fluids from escaping the fault core during rapid seismic fault motion, and consequently favoring thermal pressurization in the relatively shallow fault zone (e.g., < 5 km, Fig. 14a, b).

We observed several microstructures that are inferred to be form with the presence of fluids during fault motion. First, injection gouge veins were observed to be present in the fractures near the slip zones (Fig. 6a). Injection gouge veins or ultracataclastic veins have also been found in other outcrops of the YBF (e.g., Lin, 2011; Chen et al., 2013c; Wang et al., 2014). If enough water is present in the fault zone (most likely at the shallow depths, Chen et al., 2013c), the gouges may get fluidized such that they would behave like a flowing material, which can easily inject into fractures and forming the gouge veins (e.g., Lin, 2011; Rowe et al., 2012). Second, abundant micro-pores are widespread in the clay matrix of the fault gouges (Fig. 5d), similar to that observed in other faults such as the San Andreas fault and Chelungpu fault (Janssen et al., 2011, 2014). The presence of high fluid pressure may help explain how micro-pores in clay-rich fault gouges can persist at depths (Holdsworth et al., 2011; Janssen et al., 2011). Third, the CCAs (Fig. 5e), which has been taken as a significant evidence for the accretion of fine-grained clays to core aggregates during coseismic fluidization process (e.g., Boutareaud et al., 2010; Ferri et al., 2010; Niemeijer et al., 2012; Janssen et al., 2014, 2015; Rowe and Griffith, 2015), was widely observed in the gouges. The widespread presence of these structures essentially indicates that considerable amount of fluids exist and strong rock fluidization occurring in the slip zone during fault motion. Rock fluidization occurs because of rock pulverization with the presence of fluids, which usually results in a transient reduction in normal stress on the fault (Ujiie et al., 2007) and low shear resistance during seismic faulting (Brodsky et al., 2009).

6.3.2. Implication for dynamic weakening

Coseismic slip weakening has long been a hotly debated topic for large earthquakes. An extremely low friction coefficient (as low as 0.02) for the PSZ of the YBF was obtained from the post-seismic temperature measurement in the WFSD-1 borehole (Li et al., 2015). Several mechanisms have been proposed to explain the slip weakening associated with the Wenchuan earthquake. First, the low friction behavior in the YBF may be explained by the high clay content or enrichment of carbonaceous and graphite in the gouges (Togo et al., 2011; Kuo et al., 2014). Second, the high-velocity frictional behavior of fault gouges collected from several outcrops along the YBF show consistently low dynamic friction (0.1–0.2) at dry conditions (e.g., Hou et al., 2012; Yao et al., 2013; Chen et al., 2013a). However, none of these weakening mechanisms can explain the extremely low friction (0.02). One possible mechanism is thermal pressurization (Sibson, 1973; Mase and Smith, 1987; Wibberley and Shimamoto, 2005). Previous numerical modeling studies performed at the Zhaojiagou (Chen et al., 2013a) and Pingxi (Chen et al., 2013c) outcrops indicated that thermal pressurization might have played an important role in causing the dynamic weakening in the sedimentary strata during the fault motion of the Wenchuan earthquake. It is of great interest to see if the same mechanism applies for the granitic rocks (GR outcrop) where the 2008 Wenchuan earthquake most likely nucleated (Chen et al., 2009).

As aforementioned, the low permeability, high porosity, and large pressure sensitivity of the fault gouges imply a high potential for the buildup of excess pore pressure at depths. Regarding this issue, here, using the fluid transport properties obtained in this study and realistic parameters related to the Wenchuan earthquake, we provide a robust quantitative analysis. We consider a one-dimensional hydrothermal diffusion model for a thermal pressurization process that is perpendicular to the fault plane. The occurrence of this thermal pressurization process depends predominately on the relative rates of thermal and fluid diffusion in the principal slip zone. Following Mase and Smith (1987), the hydraulic diffusivity (D_h) and thermal diffusivity (D_t) can be written as:

$$D_h = k/\eta\beta \tag{1}$$

$$D_t = K/\rho c \tag{2}$$

In a given time scale (t), the hydraulic and thermal diffusion length (L_h and L_t) are defined as:

$$L_h = 2(D_h t)^{1/2} \tag{3}$$

$$L_t = 2(D_t t)^{1/2} \tag{4}$$

The thermal pressurization coefficient (ψ), characterizing the increase in fluid pressure per unit change in temperature, is defined as the ratio of fluid volume expansivity to the storage capacity:

$$\psi = \varphi(\alpha_f - \alpha_m)/\beta_s \tag{5}$$

The characteristic time (t_0) controlling the rate of thermal pressurization in a principal slip zone is:

$$t_0 = \rho c(W/2)/(\mu_d \psi V) \tag{6}$$

where k is permeability, η is viscosity of fluid, β is compressibility of fault rocks, β_s is specific storage of fault rocks, K is thermal conductivity, ρ is density of fault rocks, c is heat capacity of fault rocks, φ is porosity, α_f is expansivity of pore fluid, α_m is mineral expansivity, W is the width of the principal slip gouge zone (the YGG), μ_d is dynamic friction coefficient of the fault gouge, and V is coseismic slip velocity.

Based on the above considerations, the occurrence of coseismic thermal pressurization needs to satisfy the following three conditions: 1) The hydraulic diffusion length smaller than half width of the gouge zone, $L_h < W/2$; 2) The hydraulic diffusion time bigger than duration time of seismic slip, $t_f = (W/2)^2/D_h > t_e$; 3) The hydraulic diffusion length smaller than thermal conduction length, $L_h < L_t$, that is $D_h < D_t$. Here, t_f and t_e are hydraulic diffusion time and duration time of coseismic slip, respectively.

All the parameters in the above equations are listed in Table 3. In particular, from the seismic wave inversion, the co-seismic slip time and average slip velocity around the GR outcrop during the Wenchuan earthquake are about 10 s and 1.25 $m \cdot s^{-1}$, respectively (Zhang et al., 2009). An initial temperature of 80 °C is assumed according to the geothermal gradient measured in the WFSD-1 borehole (20 °C/km, Li et al., 2015). Constant values of viscosity and thermal expansivity of pure water at 80 °C are used (Table 3). Average dynamic friction coefficient (μ_d) is set to be 0.11 (Hou et al., 2012; Yao et al., 2013). To evaluate the effects of slip zone thickness and further the critical thickness over which thermal pressurization would be less important, various slip zone thicknesses from 0.5 mm to 50 mm are investigated.

Fig. 15 presents the hydraulic diffusion lengths (L_h) calculated with laboratory measured hydraulic data in the present study, plotted against the fault zone depth. The results show that the L_h decreases with increasing depth and is always smaller than half thickness of the slip zone except for extremely narrow slip zones (i.e., < 2 mm) or at very shallow depths (i.e., < 1 km). Further analyses indicate that the three conditions mentioned above can be satisfied when $k < 6.47 \times 10^{-20}$ m^2. According to our permeability measurement results for the YGG (Fig. 9e), thermal pressurization is expected to be significant when P_e exceeds 45 MPa, which corresponds to depths > 2.7 km, assuming a hydrostatic and lithostatic pressure gradient. This result is consistent with those at the Zhaojiagou and Pingxi outcrops (Chen et al., 2013a, 2013c). These analyses indicate that the permeability of the YBF at the GR site is sufficiently low at depths below 2.7 km to trap the frictional heated fluids within the PSZ during the Wenchuan earthquake. In such circumstance, pressurization and pore dilatation are the main mechanisms for accommodating the heating of pore fluids, and it is plausible to assume negligible fluid mass loss during the faulting process.

Table 3
Parameters and their values used for thermal pressurization modeling.

Parameter	Symbol	Value	Unit	Reference
Porosity of the gouge	φ	$0.23P_e^{-0.15}$	%	This study
Specific storage of the gouge	β_s	$4.93 \times 10^{-10}\exp(-0.0239P_e)$	Pa^{-1}	This study
Particle density of the gouge[a]	ρ_g	2780	$kg{\cdot}m^{-3}$	This study
Bulk density of the gouge[b]	ρ	2343	$kg{\cdot}m^{-3}$	This study
Compressibility of the gouge	β	4.71×10^{-10}	Pa^{-1}	This study
Specific heat of the gouge[c]	c	1224	$J{\cdot}kg^{-1}{\cdot}K^{-1}$	Arithmetic mean method
Thermal conductivity of gouge[d]	K	2.03	$W{\cdot}m^{-1}{\cdot}K^{-1}$	Arithmetic mean method
Viscosity of fluid[e]	η	3.54×10^{-4}	Pa·s	NIST, at temperature of 80 °C
Thermal expansion of fluid	α_f	5.0×10^{-4}	K^{-1}	Fine and Millero, 1973
Thermal expansion of mineral	α_m	2.2×10^{-5}	K^{-1}	Bayer, 1973
Compressibility of fluid	β_f	4.3×10^{-10}	Pa^{-1}	Fine and Millero, 1973
Width of the gouge zone	W	0.1	m	Duan et al., 2016
Dynamic friction[f]	μ_d	0.11 or DD		Hou et al., 2012; Yao et al., 2013
Coseismic slip rate	V	1.25	$m{\cdot}s^{-1}$	Zhang et al., 2009
Duration of coseismic slip	t_e	10–20	s	Zhang et al., 2009

[a] Particle density (ρ_g) was measured by the water pycnometer method (Blake and Hartge, 1986).
[b] Bulk density (ρ) was calculated based on the measured particle density and porosity (φ) by $\rho = (1 - \varphi)\rho_g$.
[c] Specific heat was obtained by the arithmetic mean method (e.g., Tanikawa et al., 2016) based on the XRD measured mineral composition data, porosity data and specific heat of monomineral. Specific heat data of minerals are obtained from the website at, http://www.engineeringtoolbox.com/specific-heat-solids-d_154.html.
[d] Thermal conductivity was obtained by arithmetic mean method based on the measured mineral composition data, porosity data and thermal conductivity of data monomineral. Thermal conductivity data of minerals are from Horai (1971) and Midttømme et al. (1998).
[e] Viscosity of fluid was obtained from the website of National Institute of Standards and Technology (NIST) at, http://webbook.nist.gov/chemistry/fluid/.
[f] Dynamic friction is displacement dependent (DD) and is assigned as $\mu_d = \mu_{ss} + (\mu_p - \mu_{ss})\exp((\ln 0.05)d/d_c)$, where averaged parameters of steady state friction μ_{ss}, peak friction μ_p and d_c are 0.11, 0.7 and 0.1, respectively, determined by high velocity friction experiments (Hou et al., 2012; Yao et al., 2013).

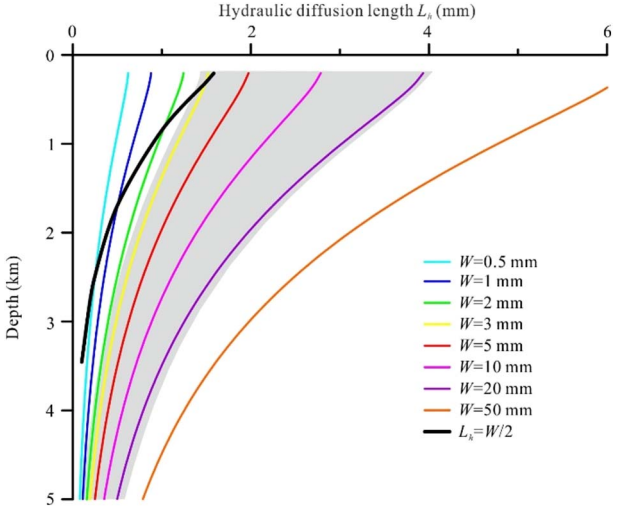

Fig. 15. Hydraulic diffusion lengths (L_h) during thermal pressurization as a function of fault zone depth. Cases are shown for various slip zone thickness (W). The L_h is always smaller than the half thickness of slip zone ($W/2$) except for extremely narrow slip zones (e.g., < 2 mm) or at extremely shallow depths (e.g., < 1–2 km). The shaded area indicates the cases for typical coseismic slip zone thicknesses of the Wenchuan earthquake observed in several outcrops along the Yingxiu-Beichuan Fault (Lin, 2011; Togo et al., 2011; Li et al., 2013).

To further investigate the effect(s) of thermal pressurization on the dynamic weakening observed, we use the analytical solutions given by Bizzarri and Cocco (2006) to calculate the coseismic temperature (ΔT) and pore pressure (ΔP) rises:

$$\Delta T(t) = \frac{V}{\rho c W}\int_0^{t-\varepsilon} \mathrm{erf}\left(\frac{W}{4\sqrt{\chi(t-t')}}\right)\mu_d\sigma_n^{eff}(t')dt' \quad (7)$$

$$\Delta P(t) = \frac{\gamma V}{W}\int_0^{t-\varepsilon}\left\{-\frac{\chi}{\omega-\chi}\mathrm{erf}\left(\frac{W}{4\sqrt{\chi(t-t')}}\right) + \frac{\omega}{\omega-\chi}\mathrm{erf}\left(\frac{W}{4\sqrt{\omega(t-t')}}\right)\right\}\mu_d\sigma_n^{eff}(t')dt' \quad (8)$$

where $\chi = K/\rho c$, $\gamma = \alpha_f/(\beta_f\rho c)$, $\omega = k/(\eta\beta_f\varphi)$, β_f is compressibility of fluid, σ_n^{eff} is effective normal stress, erf() is error function, ε is an arbitrarily small positive number and μ_d is dynamic friction coefficeint. In this case, dynamic friction is let evolve with slip displacement following typical high velocity friction data of fault gouges from the YBF (Table 3, Yao et al., 2013; Hou et al., 2012; Chen et al., 2013a). The least constrained parameter in the above equations is the slip zone thickness. The YGG, as inferred to be the PSZ of the Wenchuan earthquake, was measured to be 10 cm-thick in both the surface outcrop and the drilling cores (Duan et al., 2016). This thickness is larger than typical slip zone width, and was inferred to be an accumulation of several earthquakes according to microstructural analyses (Duan et al., 2016). The investigation of the surface rupture zones and the WFSD-1 borehole suggested that coseismic slip of Wenchuan earthquake can be localized within a few millimeters, i.e. 3 mm–7 mm (Lin, 2011; Chen et al., 2013a; Togo et al., 2011; Li et al., 2013). To account this effect, various slip zone thicknesses from 3 mm to 100 mm are investigated. Except where otherwise stated, other parameters are the same as that used in Eqs. (1)–(6) (Table 3). The calculation is at 3 km depth.

The calculated temperature and pore pressure rises caused by thermal pressurization are shown in Fig. 16a and b, respectively. The results show that temperature and pore pressure increase rapidly with fault slip, and both are sensitive to the slip zone thickness (Fig. 16a, b). For instance, for a slip zone of 5 mm in thickness, the pore pressure rise on the slip surface can be as high as 44 MPa (temperature rise as 315 °C), which would cause a reduction of effective normal stress by 88%. The evolutions of apparent frictions are shown in Fig. 16c. Taking the slip zone thickness of 5 mm for example, the apparent friction is reduced to 0.02 within 3–4 s of slip, and further to 0.013 by the end of the earthquake (Fig. 16c).

As discussed in Section 6.3.1, our permeability data support the possible maintenance of high pore pressure at depths (Fig. 14c). An obvious question is whether thermal pressurization is still efficient when a high pore pressure exists before the fault slip? To investigate this effect, we use a low friction coefficient of 0.02. The same value of friction was estimated from the in-situ temperature measurement results (Li et al., 2015). In this low friction case, > 30 MPa of pore pressure rise can be still predicted at 3 km depth, causing a 60% reduction in effective normal stress (see the black dashed line in Fig. 16b).

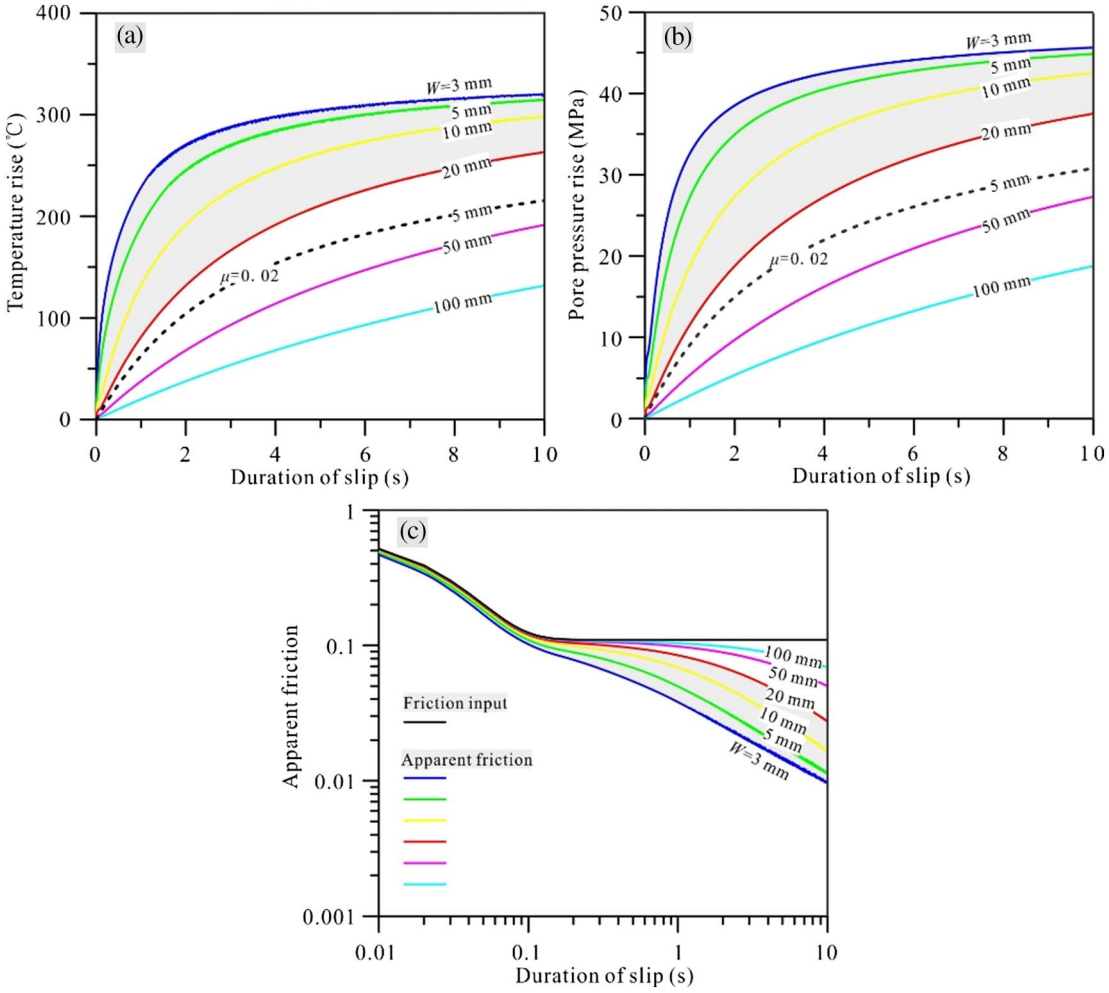

Fig. 16. Modeling results of thermal pressurization during the Wenchuan earthquake at the Golden River. (a–b) Results of temperature and pore pressure rises during thermal pressurization. (c) The evolution of apparent friction during thermal pressurization. Cases are shown for various thicknesses of slip zone (W) range from 3 mm to 100 mm. The shaded areas indicate the cases for typical coseismic slip zone thickness of the Wenchuan earthquake observed in several outcrops along the Yingxiu-Beichuan fault (Lin, 2011; Togo et al., 2011; Li et al., 2013). Dynamic friction (input) is assigned to evolve with displacement according to high velocity experiment data (Hou et al., 2012; Yao et al., 2013). In panels (a) and (b), the results obtained using a constant friction coefficient of 0.02 (Li et al., 2015), as presented by the black dash lines, are added for comparison.

Therefore, even if high pore pressure exists at depths before the earthquake, thermal pressurization can also occur and generate significant stress drop. The above results consistently show that the PSZ at the GR site is low permeable enough to generate effective thermal pressurization during the coseismic slip. Detailed calculation based on the hydraulic data measured in the present study show that fluid pressurization should have occurred extensively at depths during the Wenchuan earthquake and can help explain the extremely low friction obtained by post-seismic temperature measurement (Li et al., 2015), which offers an expelling explanation to the dynamic weakening observed for the earthquake.

7. Conclusions

We conducted microstructural and mineralogical analyses, and fluid transport properties (including permeability, porosity, and specific storage) experiments on the fault rocks collected from shallow boreholes drilled into a granitic rupture zone on the YBF, to gain better understand on the hydraulic conduction features and dynamic weakening mechanism for the Wenchuan earthquake. The main conclusions are summarized as follow:

(1) Permeability structure of the YBF at the outcrop studied consists of ultra-low permeable fault core and host rocks and high permeable damage zones. At P_e of 165 MPa, the damage zones have permeabilities from 5.0×10^{-21} m^2 to 1.2×10^{-17} m^2, and the fault core samples are between 2.1×10^{-22} m^2 and 3.1×10^{-19} m^2. The hydraulic profile thus exhibits a typical conduit/barrier structure, with fluid flow being trapped in the damage zones, and tending to migrate parallel to the fault plane as the low permeable fault core may prevent fluids from flowing across it.

(2) Hydraulic conductions of the fault rocks are controlled predominately by cracks and micro-pores therein developed. Microstructural observations show that the fault rocks heal through fluid-associated mineral precipitation and cementation that lead to crack closure, and probably enhanced by pressure solution. We propose that the interplay between mechanical cataclasis (grain size reduction, creation of cracks) and fluid-rock interactions (formation of clays, precipitation of hydrothermal minerals) controls the hydraulic structure and its response to the fault zone evolution.

(3) We measured extremely low permeabilities but high porosities and specific storages for the gouges, the cemented granitic cataclasites which are inferred to be equivalent to the rocks at depth where the Wenchuan earthquake nucleated also have low permeabilities, indicating a high capability for the buildup of excess pore fluid pressure at depths. Based on the transport data, we note that the PSZ of the Wenchuan earthquake at the GR site is low permeable enough to prevent frictional heated fluids from escaping the slip

zone to generate high pore pressure and cause dynamic weakening during coseismic slip.

Acknowledgements

This study was supported by the National Natural Science Foundation of China (Grant No. 41602227; 41372202) and Public Service Funds for Earthquake Studies (Grant No. 201508018). We thank editor Kelin Wang for efficient handling of the manuscript, and two anonymous reviewers for thorough and constructive reviews.

References

Bayer, G., 1973. Thermal expansion anisotropy of oxide compounds. Proc. Br. Ceram. Soc. 22, 39–53.
Behnsen, J., Faulkner, D.R., 2011. Water and argon permeability of phyllosilicate powders under medium to high pressure. J. Geophys. Res. 116, B12203.
Bernabé, Y., Mok, U., Evans, B., Herrmann, F.J., 2004. Permeability and storativity of binary mixtures of high- and low-permeability materials. J. Geophys. Res. Solid Earth 109 (B12) (1978–2012).
Bernabé, Y., Mok, U., Evans, B., 2006. A note on the oscillating flow method for measuring rock permeability. Int. J. Rock Mech. Min. Sci. 43 (2), 311–316.
Bizzarri, A., Cocco, M., 2006. A thermal pressurization model for the spontaneous dynamic rupture propagation on a three-dimensional fault: 1. Methodological approach. J. Geophys. Res. Solid Earth 111 (B5).
Blake, G.R., Hartge, K.H., 1986. Particle density. In: Methods of Soil Analysis: Part 1—Physical and Mineralogical Methods, pp. 377–382 (methodsofsoilan1).
Boulton, C., Carpenter, B.M., Toy, V., Marone, C., 2012. Physical properties of surface outcrop cataclastic fault rocks, Alpine Fault, New Zealand. Geochem. Geophys. Geosyst. 13, Q01018. http://dx.doi.org/10.1029/2011GC003872.
Boutareaud, S., Boullier, A.M., Andreani, M., Calugaru, D.G., Beck, P., Song, S.R., Shimamoto, T., 2010. Clay clast aggregates in gouges: new textural evidence for seismic faulting. J. Geophys. Res. Solid Earth 115 (B2) (1978–2012).
Boutt, D.F., Saffer, D., Doan, M.L., et al., 2012. Scale dependence of in-situ permeability measurements in the Nankai accretionary prism: the role of fractures. Geophys. Res. Lett. 39, L07302. http://dx.doi.org/10.1029/2012GL051216.
Brodsky, E.E., Rowe, C.D., Meneghini, F., Moore, J.C., 2009. A geological fingerprint of low-viscosity fault fluids mobilized during an earthquake. J. Geophys. Res. Solid Earth 114 (B1).
Burchfiel, B.C., Chen, Z.L., Liu, Y.P., Royden, L.H., 1995. Tectonics of the Longmen Shan and Adjacent Regions, Central China. Int. Geol. Rev. 37 (8), 661–735.
Byerlee, J., 1990. Friction, overpressure and fault normal compression. Geophys. Res. Lett. 17 (12), 2109–2112.
Byerlee, J.D., 1993. Model for episodic flow of high-pressure water in fault zones before earthquakes. Geology 21 (4), 303–306.
Caine, J.S., Evans, J.P., Forster, C.B., 1996. Fault zone architecture and permeability structure. Geology 24, 1025–1028.
Carpenter, B.M., Kitajima, H., Sutherland, R., Townend, J., Toy, V.G., Saffer, D.M., 2014. Hydraulic and acoustic properties of the active Alpine Fault, New Zealand: Laboratory measurements on DFDP-1 drill core. Earth Planet. Sci. Lett. 390, 45–51.
Chen, J.H., Liu, Q.Y., Li, S.C., et al., 2009. Seismotectonic study by relocation of the Wenchuan MS 8.0 earthquake sequence, Chinese. J. Geophys. 52 (2), 390–397 (in Chinese with English abstract).
Chen, J.Y., Yang, X.S., Dang, J.X., He, C.R., Zhou, Y.S., Ma, S.L., 2011. Internal structure and permeability of Wenchuan earthquake fault. Chin. J. Geophys. 54 (7), 1805–1816 (in Chinese with English abstract).
Chen, J.Y., Yang, X.S., Duan, Q.B., et al., 2013a. Importance of thermochemical pressurization in the dynamic weakening of Longmenshan fault during the 2008 Wenchuan earthquake: inference from experiments and modeling. J. Geophys. Res. 118, 4145–4169.
Chen, J.Y., Yang, X.S., Ma, S.L., et al., 2013b. Mass removal and clay mineral dehydration/rehydration in carbonate-rich surface exposures of the 2008 Wenchuan Earthquake fault: geochemical evidence and implications for fault zone evolution and coseismic slip. J. Geophys. Res. Solid Earth 118, 474–496.
Chen, J.Y., Yang, X.S., Yao, L., et al., 2013c. Frictional and transport properties of the 2008 Wenchuan Earthquake fault zone: implications for coseismic slip-weakening mechanisms. Tectonophysics 603, 237–256.
Chen, J.Y., Yang, X.S., Duan, Q.B., Peach, C., 2015. Integrated measurements of permeability, effective porosity and specific storage of core samples using water as the pore fluid. Int. J. Rock Mech. Min. Sci. 79, 55–62. http://dx.doi.org/10.1016/j.ijrmms.2015.08.007.
Chen, J.Y., Yang, X.S., Ma, S.L., Yang, T., Niemeijer, A., 2016. Hydraulic properties of samples retrieved from the Wenchuan earthquake fault scientific drilling project hole-1 (WFSD-1) and the surface rupture zone: Implications for coseismic slip weakening and fault healing. Geochem. Geophys. Geosyst. 17. http://dx.doi.org/10.1002/2016GC006376.
Chester, F.M., Logan, J., 1986. Implications for mechanical properties of brittle faults from observations of the Punchbowl fault zone, California. Pure Appl. Geophys. 124, 79–106.
Chester, F.M., Evans, J.P., Biegel, R.L., 1993. Internal structure and weakening mechanisms of the San Andreas fault. J. Geophys. Res. Solid Earth 98, 771–786.
David, C., Wong, T.F., Zhu, W., et al., 1994. Laboratory measurement of compaction-induced permeability change in porous rocks: Implications for the generation and maintenance of pore pressure excess in the crust. Pure Appl. Geophys. 143, 425–456.
Duan, Q.B., Yang, X.S., 2014. Experimental studies on gas and water permeability of fault rocks from the rupture of the 2008 Wenchuan earthquake, China. Sci. China Earth Sci. 57 (11), 2825–2834. http://dx.doi.org/10.1007/s11430-014-4948-7.
Duan, Q.B., Yang, X.S., Ma, S.L., Chen, J.Y., Chen, J.Y., 2016. Fluid-rock interactions in seismic faults: implications from the structures and mineralogical and geochemical compositions of drilling cores from the rupture of the 2008 Wenchuan earthquake, China. Tectonophysics 666, 260–280. http://dx.doi.org/10.1016/j.tecto.2015.11.008.
Engelder, T., 1987. Joints and shear fractures in rock. Fract. Mech. Rock 27–69.
Evans, J.P., Forster, C.B., Goddard, J.V., 1997. Permeability of fault-related rocks, and implications for hydraulic structure of fault zone. J. Struct. Geol. 19, 1393–1404.
Faulkner, D.R., Rutter, E.H., 2000. Comparisons of water and argon permeability in natural clay-bearing fault gouge under high pressure at 20 °C. J. Geophys. Res. 105, 16415–16426.
Faulkner, D.R., Lewis, A.C., Rutter, E.H., 2003. On the internal structure and mechanics of large strike-slip fault zones: field observations of the Carboneras fault in southeastern Spain. Tectonophysics 367 (3), 235–251.
Faulkner, D.R., Jackson, C., Lunn, R., et al., 2010. A review of recent developments concerning the structure, mechanics and fluid flow properties of fault zones. J. Struct. Geol. 32, 1557–1575.
Ferri, F., Di Toro, G., Hirose, T., Shimamoto, T., 2010. Evidence of thermal pressurization in high-velocity friction experiments on smectite-rich gouges. Terra Nova 22 (5), 347–353.
Fine, R.A., Millero, F.J., 1973. Compressibility of water as a function of temperature and pressure. J. Chem. Phys. 59 (10), 5529–5536.
Fischer, G.J., Paterson, M.S., 1992. Measurements of permeability and storage capacity in rocks during deformation at high temperature and pressure. In: Evans, B., Wong, T.-F. (Eds.), Fault Mechanics and Transport Properties of Rocks. Academic Press, New York, pp. 213–252.
Gratier, J.P., Favreau, P., Renard, F., 2003. Modeling fluid transfer along California faults when integrating pressure solution crack sealing and compaction processes. J. Geophys. Res. Solid Earth 108 (B2). http://dx.doi.org/10.1029/2001JB000380.
Gratier, J.P., Richard, J., Renard, F., Mittempergher, S., Doan, M.L., Di Toro, G., Hadizadeh, J., Boullier, A.-M., 2011. Aseismic sliding of active faults by pressure solution creep: evidence from the San Andreas Fault Observatory at Depth. Geology 12, 1131–1134.
Hancock, P.L., Maddock, R., Zoback, M.L., Skipp, B., Vita-Finzi, C., 1991. Determining contemporary stress directions from neotectonic joint systems. Philos. Trans. R. Soc. London A Math. Phys. Eng. Sci. 337 (1645), 29–40.
Hickman, S., Sibson, R., Bruhn, R., 1995. Introduction to special section: mechanical involvement of fluids in faulting. J. Geophys. Res. 100, 12831–12840.
Holdsworth, R., Van Diggelen, E., Spiers, C., et al., 2011. Fault rocks from the SAFOD core samples: implications for weakening at shallow depths along the San Andreas Fault, California. J. Struct. Geol. 33, 132–144.
Horai, K.I., 1971. Thermal conductivity of rock-forming minerals. J. Geophys. Res. 76 (5), 1278–1308.
Hou, L., Ma, S., Shimamoto, T., Chen, J., Yao, L., Yang, X., Okimura, Y., 2012. Internal structures and high-velocity frictional properties of a bedding-parallel carbonate fault at Xiaojiaqiao outcrop activated by the 2008 Wenchuan earthquake. Earthq. Sci. 25, 197–217.
Hubbard, C.R., Evans, E.H., Smith, D.K., 1976. The reference intensity ratio, I/Ic, for computer simulated powder patterns. J. Appl. Crystallogr. 9 (2), 169–174.
Janssen, C., Wirth, R., Reinicke, A., et al., 2011. Nanoscale porosity in SAFOD core samples (San Andreas Fault). Earth Planet. Sci. Lett. 301, 179–189.
Janssen, C., Wirth, R., Wenk, H.R., Morales, L., Naumann, R., Kienast, M., Song, S.R., Dresen, G., 2014. Faulting processes in active faults – evidences from TCDP and SAFOD drill core samples. J. Struct. Geol. 65, 100–116.
Janssen, C., Naumann, R., Morales, L., Wirth, R., Rhede, D., Dresen, G., 2015. Co-seismic and/or a-seismic microstructures of JFAST 343 core samples from the Japan Trench. Mar. Geol. 362, 33–42.
Kitagawa, Y., Fujimori, K., Koizumi, N., 2002. Temporal change in permeability of the rock estimated from repeated water injection experiments near the Nojima fault in Awaji Island, Japan. Geophys. Res. Lett. 29, 121–124.
Kouketsu, Y., Shimizu, I., Wang, Y., Yao, L., Ma, S., Shimamoto, T., 2017. Raman spectra of carbonaceous materials in a fault zone in the Longmenshan thrust belt, China; comparisons with those of sedimentary and metamorphic rocks. Tectonophysics. http://dx.doi.org/10.1016/j.tecto.2017.01.015.
Kranz, R.L., Saltzman, J.S., Blacic, J.D., 1990. Hydraulic diffusivity measurements on laboratory samples using an oscillating pore pressure method. Int. J. Rock Mech. Min. Sci. Geomech. Abstr. 27, 345–352.
Kuo, L.W., Li, H.B., Smith, S.A.F., Di Toro, G., Suppe, J., Song, S.R., Nielsen, S., Sheu, H.S., Si, J.L., 2014. Gouge graphitization and dynamic fault weakening during the 2008 Mw 7.9 Wenchuan earthquake. Geology 42, 47–50.
Li, H.B., Wang, H., Xu, Z.Q., Si, J.L., Pei, J.L., Li, T.F., Huang, Y., Song, S.R., Kuo, L.W., Sun, Z.M., Chevalier, M., Liu, D.L., 2013. Characteristics of the fault-related rocks, fault zones and the principal slip zone in the Wenchuan Earthquake Fault Scientific Drilling Project Hole-1 (WFSD-1). Tectonophysics 584, 23–42.
Li, H.B., Xue, L., Brodsky, E.E., Mori, J., Fulton, P.M., Wang, H., Kano, Y., Yun, K., Harris, R.N., Gong, Z., Li, C.L., Si, J.L., Sun, Z.M., Pei, J.L., Zheng, Y., Xu, Z.Q., 2015. Long-term temperature records following the Mw 7.9 Wenchuan (China) earthquake consistent with low friction. Geology 43 (2), 163–166.
Lin, A., 2011. Seismic slip recorded by fluidized ultracataclastic veins formed in a coseismic shear zone during the 2008 Mw 7.9 Wenchuan earthquake. Geology 39, 547–550.

Liu, J., Li, H., Zhang, J., et al., 2016. Origin and formation of carbonaceous material veins in the 2008 Wenchuan earthquake fault zone. Earth Planet. Space 68 (19). http://dx.doi.org/10.1186/s40623-016-0399-z.
Lockner, D., Naka, H., Tanaka, H., et al., 2000. Permeability and strength of core samples from the Nojima fault of the 1995 Kobe earthquake. Proceedings of the international workshop on the Nojima fault core and borehole data analysis. US Geol. Sur. 22–23.
Ma, Y.W., Wang, G.Q., Hu, X.W., 1996. Tectonic deformation of Pengguan complex as a nappe. Acta Geol. Sichuan 16 (2), 110–114 (in Chinese with English abstract).
Mase, C.W., Smith, L., 1987. Effects of frictional heating on the thermal, hydrologic, and mechanical response of a fault. J. Geophys. Res. Solid Earth 92 (B7), 6249–6272.
Midttømme, K., Roaldset, E., Aagaard, P., 1998. Thermal conductivity of claystones and mudstones selected from England. Clay Miner. 33 (1), 131–145.
Mitchell, T.M., Faulkner, D.R., 2012. Towards quantifying the matrix permeability of fault damage zones in low porosity rocks. Earth Planet. Sci. Lett. 339, 24–31.
Mizoguchi, K., Hirose, T., Shimamoto, T., et al., 2008. Internal structure and permeability of the Nojima fault, southwest Japan. J. Struct. Geol. 30, 513–524.
Molli, G., Cortecci, G., Vaselli, L., Ottria, G., Cortopassi, A., Dinelli, E., Mussi, M., Barbieri, M., 2010. Fault zone structure and fluid–rock interaction of a high angle normal fault in Carrara marble (NW Tuscany, Italy). J. Struct. Geol. 32, 1334–1348.
Morrow, C.A., Lockner, D.A., 1994. Permeability differences between surface-derived and deep drillhole core samples. Geophys. Res. Lett. 21 (19), 2151–2154.
Morrow, C.A., Shi, L.Q., Byerlee, J.D., 1981. Permeability and strength of San Andreas fault gouge under high pressure. Geophys. Res. Lett. 8, 325–328.
Morrow, C.A., Lockner, D.A., Moore, D.E., et al., 2014. Deep permeability of the San Andreas fault from San Andreas fault observatory at depth (SAFOD) core samples. J. Struct. Geol. 64, 99–114.
Niemeijer, A., Di Toro, G., Griffith, W.A., Bistacchi, A., Smith, S.A., Nielsen, S., 2012. Inferring earthquake physics and chemistry using an integrated field and laboratory approach. J. Struct. Geol. 39, 2–36.
Noda, H., Shimamoto, T., 2005. Thermal pressurization and slip-weakening distance of a fault: an example of the Hanaore fault, southwest Japan. Bull. Seismol. Soc. Am. 95 (4), 1224–1233.
Pirlet, H., Wehrmann, L.M., Brunner, B., et al., 2010. Diagenetic formation of gypsum and dolomite in a cold–water coral mound in the Porcupine Seabight, off Ireland. Sedimentology 57 (3), 786–805.
Polak, A., Elsworth, D., Yasuhara, H., et al., 2003. Permeability reduction of a natural fracture under net dissolution by hydrothermal fluids. Geophys. Res. Lett. 30 (20). http://dx.doi.org/10.1029/2003GL017575.
Ran, Y., Shi, X., Wang, H., Chen, L., Chen, J., Liu, R., Gong, H., et al., 2010. The maximum vertical co-seismic displacement and the style of deformation associated with the 2008 Wenchuan earthquake. Chin. Sci. Bull. 54 (9), 841–850.
Rice, J.R., 1992. Fault stress states, pore pressure distributions, and the weakness of the San Andreas fault. International. Geophysics 51, 475–503.
Rice, J.R., 2006. Heating and weakening of faults during earthquake slip. J. Geophys. Res. 111, B05311. http://dx.doi.org/10.1029/2005JB004006.
Rowe, C.D., Griffith, W.A., 2015. Do faults preserve a record of seismic slip: a second opinion. J. Struct. Geol. 78, 1–26.
Rowe, C.D., Kirkpatrick, J.D., Brodsky, E.E., 2012. Fault rock injections record paleo-earthquakes. Earth Planet. Sci. Lett. 335, 154–166.
Scholz, C.H., 2002. The Mechanics of Earthquakes and Faulting, 2nd ed. Cambridge Univ. Press, Cambridge, U. K. (471 pp.).
Shi, Y., Wang, C.Y., 1986. Pore pressure generation in sedimentary basins: overloading versus aquathermal. J. Geophys. Res. 91 (B2), 2153–2162.
Sibson, R.H., 1973. Interactions between temperature and pore-fluid pressure during earthquake faulting and a mechanism for partial or total stress relief. Nature 243, 66–68.
Sibson, R.H., 1977. Fault rocks and fault mechanisms. J. Geol. Soc. 133, 191–213.
Sibson, R.H., 1992. Implications of fault-valve behavior for rupture nucleation and recurrence. Tectonophysics 211 (1), 283–293.
Sibson, R.H., Robert, F., Poulsen, H., 1988. High-angle reverse faults, fluid-pressure cycling and mesothermal gold-quartz deposits. Geology 16, 551–555.
Solum, J.G., van der Pluijm, B.A., Peacor, D.R., Warr, L.N., 2003. Influence of phyllosilicate mineral assemblages, fabrics, and fluids on the behavior of the Punchbowl fault, southern California. J. Geophys. Res. Solid Earth 108 (B5).
Solum, J.G., Hickman, S.H., Lockner, D.A., Moore, D.E., van der Pluijm, B.A., Schleicher, A.M., Evans, J.P., 2006. Mineralogical characterization of protolith and fault rocks from the SAFOD main hole. Geophys. Res. Lett. 33 (21). http://dx.doi.org/10.1029/2006GL027285.
Takahashi, M., Mizoguchi, K., Kitamura, K., Masuda, K., 2007. Effects of clay content on the frictional strength and fluid transport property of faults. J. Geophys. Res. Solid Earth 112 (B8).
Tanikawa, W., Shimamoto, T., 2009. Frictional and transport properties of the Chelungpu fault from shallow borehole data and their correlation with seismic behavior during the 1999 Chi-Chi earthquake. J. Geophys. Res. Solid Earth 114 (B1). http://dx.doi.org/10.1029/2008JB005750.
Tanikawa, W., Sakaguchi, M., Hirono, T., et al., 2009. Transport properties and dynamic processes in a fault zone from samples recovered from TCDP Hole B of the Taiwan Chelungpu Fault Drilling Project. Geochem. Geophys. Geosyst. 10 (4). http://dx.doi.org/10.1029/2008GC002269.
Tanikawa, W., Tadai, O., Morita, S., Lin, W., Yamada, Y., Sanada, Y., Moe, K., Kubo, Y., Inagaki, F., 2016. Thermal properties and thermal structure in the deep-water coalbed basin off the Shimokita Peninsula, Japan. Mar. Pet. Geol. 73, 445–461.
Togo, T., Shimamoto, T., Ma, S.L., Wen, X.Z., He, H.L., 2011. Internal structure of Longmenshan fault zone at Hongkou outcrop, Sichuan, China, that caused the 2008 Wenchuan earthquake. Earthq. Sci. 24, 249–265.
Uehara, S.I., Shimamoto, T., 2004. Gas permeability evolution of cataclasite and fault gouge in triaxial compression and implications for changes in fault-zone permeability structure through the earthquake cycle. Tectonophysics 378, 183–195.
Ujiie, K., Yamaguchi, A., Kimura, G., Toh, S., 2007. Fluidization of granular material in a subduction thrust at seismogenic depths. Earth Planet. Sci. Lett. 259 (3), 307–318.
Verberne, B.A., He, C.R., Spiers, C.J., 2010. Frictional properties of sedimentary rocks and natural fault gouge from the Longmen Shan fault zone, Sichuan, China. Bull. Seismol. Soc. Am. 100, 2767–2790.
Wang, H., Li, H., Si, J., Sun, Z., Huang, Y., 2014. Internal structure of the Wenchuan earthquake fault zone, revealed by surface outcrop and WFSD-1 drilling core investigation. Tectonophysics 619–620, 101–114.
Wibberley, C.A., Shimamoto, T., 2003. Internal structure and permeability of major strike-slip fault zones: the Median Tectonic Line in Mie Prefecture, Southwest Japan. J. Struct. Geol. 25, 59–78.
Wibberley, C.A., Shimamoto, T., 2005. Earthquake slip weakening and asperities explained by thermal pressurization. Nature 436, 689–692.
Wintsch, R., Christoffersen, R., Kronenberg, A., 1995. Fluid-rock reaction weakening of fault zones. J. Geophys. Res. 100, 13021–13032.
Woodcock, N.H., Mort, K., 2008. Classification of fault breccias and related fault rocks. Geol. Mag. 145 (03), 435–440.
Wu, F.T., 1978. Mineralogy and physical nature of clay gouge. Pure Appl. Geophys. 116, 655–689.
Xu, X.W., Zhang, P.Z., Wen, X.Z., Qin, Z.L., Chen, G.H., Zhu, A.L., 2005. Features of active tectonics and recurrence behaviors of strong earthquakes in the Western Sichuan province and its adjacent regions. Seismol. Geol. 27 (3), 446–461 (in Chinese with English abstract).
Xu, X.W., Wen, X.Z., Yu, G., Chen, G., Klinger, Y., Hubbard, J., Shaw, J., 2009. Coseismic reverse-and oblique-slip surface faulting generated by the 2008 Mw 7.9 Wenchuan earthquake, China. Geology 37, 515–518.
Xue, L., Li, H.B., Brodsky, E.E., Xu, Z.Q., Kano, Y., Wang, H., Mori, J.J., Si, J.L., Pei, J.L., Zhang, W., Yang, G., Sun, Z.M., Huang, Y., 2013. Continuous permeability measurements record healing inside the Wenchuan earthquake fault zone. Science 340 (6140), 1555–1559.
Yang, T., Chen, J., Wang, H., Jin, H., 2012. Rock magnetic properties of fault rocks from the rupture of the 2008 Wenchuan earthquake, China and their implications: Preliminary results from the Zhaojiagou outcrop, Beichuan County (Sichuan). Tectonophysics 530, 331–341.
Yang, T., Yang, X.S., Duan, Q.B., Chen, J.Y., Dekkers, M.J., 2016. Rock magnetic expression of fluid infiltration in the Yingxiu-Beichuan Fault (Longmen Shan thrust belt, China). Geochem. Geophys. Geosyst. 17 (3), 1065–1085. http://dx.doi.org/10.1002/2015GC006095.
Yao, L., Ma, S., Shimamoto, T., Togo, T., 2013. Structures and high-velocity frictional properties of the Pingxi fault zone in the Longmenshan fault system, Sichuan, China, activated during the 2008 Wenchuan earthquake. Tectonophysics 599, 135–156.
Zhang, L., He, C.R., 2013. Frictional properties of natural gouges from Longmenshan fault zone ruptured during the Wenchuan Mw 7.9 earthquake. Tectonophysics 594, 149–164.
Zhang, P., Zhou, Z.Y., Xu, C.H., Zhang, Q.L., 2008. Geochemistry of Pengguan complex in the Longmenshan region, western Sichuan province, SW China: petrogenesis and tectonic implications. Geotecton. Metallog. 32, 105–116 (in Chinese with English abstract).
Zhang, Y., Feng, W.P., Xu, L.S., Zhou, C., Chen, Y.T., 2009. Spatio-temporal rupture process of the 2008 great Wenchuan earthquake. Sci. China Ser. D Earth Sci. 52 (2), 145–154.
Zhou, Y.S., He, C.R., 2009. The rheological structures of crust and mechanics of high-angle reverse fault slip for Wenchuan Ms 8.0 earthquake. Chin. J. Geophys. 52 (2), 474–484 (in Chinese with English abstract).
Zhu, W., Montesi, G.J., Wong, T., 1997. Shear-enhanced compaction and permeability reduction: triaxial extension tests on porous sandstone. Mech. Mater. 25 (3), 199–214.